学位論文(要約)

Developments of Functional Bottom-up Coordination Nanosheets (CONASHs): Bis(dipyrrinato)zinc(II) CONASH with Photoelectric Conversion and Bis(acetylacetonato)copper(II) CONASH with Molecular Recognition

（光電変換特性を有するビスジピリナト亜鉛(II)ナノシートおよび
分子認識能を有するビスアセチルアセトナト銅(II)ナノシート
による機能性ボトムアップ型配位ナノシートの展開　）

星子　健

Abstract

This thesis describes studies on designing and demonstration of bottom-up coordination nanosheets' functions. Two types of metal complex act as component molecules for the nanosheets construction; one is bis(dipyrrinato)zinc(II) and the other is bis(acetylacetonato)copper(II). These components' functions can be successfully introduced to the nanosheet to fabricate functional coordination nanosheets.

In Chapter 1, I describe the general introduction of molecular two-dimensoional (2D) materials, nanosheets. Various series of nanosheets and their functions are mentioned.

In Chapter 2, I state the fabrication and optical properties of bis(dipyrrinato)zinc(II) nanosheets (**N1**). Interfacial reaction between a three-way dipyrrin ligand (1,3,5-tris-[4'-(5-mehyl-1H-pyrrole-2-yl(5-methyl -2H-pyrrole-2-ylidene)methyl)phenyl]benzene) and zinc ions produces both multi-layer and single-layer nanosheets (**multi-layer N1** and **single-layer N1**), and the flat homogeneous single-layer area is significantly larger than other coordination nanosheets. Their morphology, constituent elements and properties are confirmed by optical microscopy, XPS, Ultraviolet/visible (UV/vis) spectroscopy, TEM/SAED, AFM, STM and electrochemical measurements. The bis(dipyrrinato)zinc(II) complex motif acts as a photofunctional moiety to exhibit photoelectric conversion ability. This is the first bottom-up coordination nanosheet to show photofunctionality.

In Chapter 3, I mention the fabrication and molecular recognition of bis(acetylacetonato)copper(II) nanosheets (**N2**). Interfacial reaction between a three-way acetylacetone ligand (1,3,5-tris-[4'-(3"-acetylacetonato)phenyl] benzene) and copper(II) ions produce both multi-layer and single-layer nanosheets (**multi-layer N2** and **single-layer N2**), and the single-layer nanosheets also reveal much larger homogeneous area than other coordination nanosheets. Their morphology, constituent elements and properties are confirmed by optical microscopy, XPS, UV/vis spectroscopy, SEM/EDX, XRD, and AFM measurements. The optical property is modulated by coordinating molecules to the coordinatively unsaturated

metal center units.

In Chapter 4, I describe the conclusion of this research.

Contents

Chapter 3 Bis(acetylacetonato)copper(II) nanosheet   77

本章については、5 年以内に雑誌等で刊行予定のため、非公開

Chapter 4 Concluding remarks   79

Acknowledgement   83

Publication List   85

Chapter 1

General introduction

1-1 Two-dimensional materials nanosheets

Nanosheets are two-dimensional planar polymeric materials with nm-scale thickness. Their two-dimensional morphology and ultrathin thickness cause unusual physical and chemical properties different from their bulk materials. It promises the nanosheets potential to become revolutionary materials in various application.

At the first stage most of nanosheet materials were obtained via dimension-reduced approach: exfoliation of three-dimensional layered bulk materials. In this method we can get the nanosheet materials by a very simple way, just exfoliating the bulk materials by a Scotch tape. These nanosheets are called top-down nanosheets. From a discovery of graphene[1] which is corresponding to a single-layer graphite, a lot of nanosheets materials such as transition metal chalcogenides, metal oxides or metal hydroxides are synthesized by this simple method.

On the other hand, recently molecule-based nanosheets, so-called bottom-up nanosheets, have been emerged. This series of nanosheets is obtained from molecular, ionic, or atomic components. These components are chemically linked together toward two-dimensional direction to form nanosheets. In the case of bottom-up nanosheets there are significant features; we can use an infinite number of components to broaden their diversities and utilities, and we can customize their structures and properties through the selection of components.
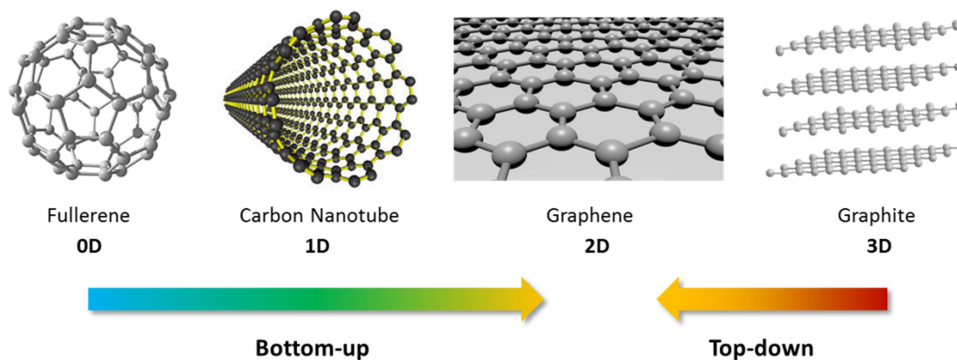

Figure 1-1-1 Two approaches of nanosheets synthesis: top-down synthesis or bottom-up synthesis

1-2 Nanosheets materials

1-2-1 Graphene and its derivatives

The breakthrough of nanosheet research came after the discovery of a very simple synthetic method of graphene in 2004[1]. Graphene was obtained by top-down exfoliation method of layered graphite with Scotch tape. Graphene is composed of sp^2-hybridized carbon atoms which is corresponding to single-layer graphite, and it has a hexagonal honeycomb structure with 1 nm ripple[2]. Derived from its unique structure, graphene possesses specific Dirac cones in the band structure. Its ultrathin structure and unique band structure produce a lot of attractive physical properties different from typical bulk materials, such as high carrier mobilities[3], large light absoptivities[4], quantum hall effect at room temperature[5], large thermal conductivity[6], and high mechanical strength[7]. These attractive properties fascinate researchers and promise various applications in electronics[1], photonics[8], spintronics[9], capacitors[10], batteries[11], solar cells[12], and filler materials[13]. Graphene is now commercially supplied by various companies.

The outstanding properties of graphene also led to the discoveries other single element's nanosheets such as silicene[14], germanene[15], stanene[16], phosphorene[17], and borophene[18].

(a)

(b)

(c)

(d)
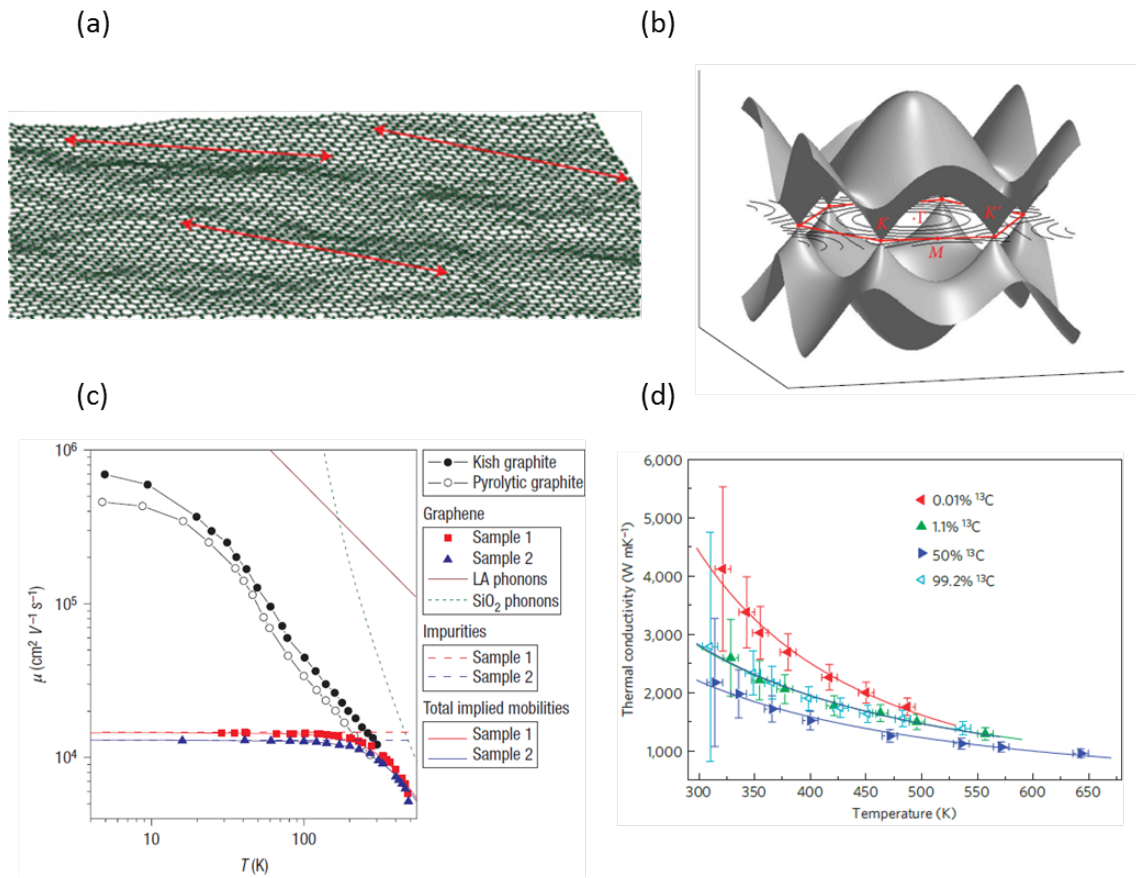
Figure 1-2-1 (a) Illustration of graphene ripple[2]. (b) First Brillouin zone and band structure of graphene[19]. (c) Temperature dependence of graphene carrier mobility[3]. (d) Thermal conductivity of graphene[6].

1-2-2 Inorganic nanosheets

The broad attention and expected utilities of graphene have stimulated researchers. They then focused on other nanosheets materials, one of which was two-dimensional transition metal dichalcogenides[20] (2D TMDs). It has a chemical composition of MX_2, where M is a transition metal (Ti, Nb, Ta, Mo, W, etc.) and X is a chalcogen atom (S, Se, Te, etc.). The single-layer 2D TMDs can be obtained by two kinds of methods: top-down exfoliation of layered bulk materials and chemical vapor deposition (CVD) method. Different from graphene, their sizable bandgap[21] is a big advantage for application in semiconducting electronics.

Group	M	X	Properties
4	Ti, Hf, Zr	S, Se, Te	Semiconducting (E_g = 0.2-2 eV). Diamagnetic.
5	V, Nb, Ta	S, Se, Te	Narrow band metals (ρ ~10^{-4} Ω.cm) or semimetals. Superconducting. Charge density wave (CDW). Paramagnetic, antiferromagnetic, or diamagnetic.
6	Mo, W	S, Se, Te	Sulfides and selenides are semiconducting (E_g ~1 eV). Tellurides are semimetallic (ρ ~10^{-3} Ω cm). Diamagnetic.
7	Tc, Re	S, Se, Te	Small-gap semiconductors. Diamagnetic.
10	Pd, Pt	S, Se, Te	Sulfides and selenides are semiconducting (E_g = 0.4 eV) and diamagnetic. Tellurides are metallic and paramagnetic. PdTe$_2$ is superconducting.

ρ, in-plane electrical resistivity.

(b)
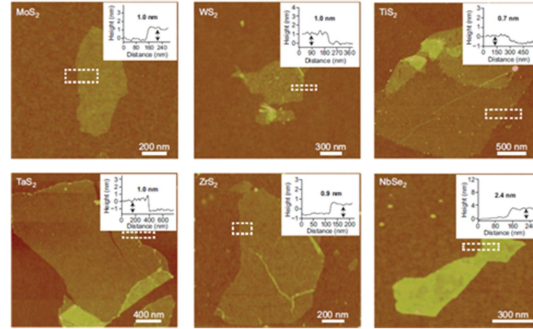
(c)

TMD	Precursor	Growth condition	Morphology
MoS$_2$	(NH$_4$)$_2$MoS$_4$* in DMF by bubbling with Ar	200 mTorr to 2 Torr at 400 °C	Hexagonal flake with 2 to 5 nm thickness
MoSe$_2$	MoCl$_5$ (heating at 255 °C) C$_8$H$_{18}$Se† (70 °C) or C$_4$H$_{10}$Se‡ (90 °C)	Atmosphere at 450 ~ 600 °C	Thin film for C$_8$H$_{18}$Se Needle-like structures for C$_4$H$_{10}$Se
WS$_2$	WOCl$_4$ (heating at 176 °C) HS(CH$_2$)$_2$SH§ (heating at 63 °C)	Atmosphere at 250 ~ 600 °C	Thin film
WSe$_2$	WOCl$_6$ (heating at 260 °C) C$_4$H$_{10}$Se‡ (heating at 70 °C)	Atmosphere at 450 ~ 600 °C	Plate-like crystallites mixed with needle-like crystal
VSe$_2$	V(NMe$_2$)$_4$‖ (heating at 130 °C) C$_8$H$_{18}$Se† (heating at 90 °C)	Atmosphere at 250 ~ 500 °C	Thin hexagonal platelets
TiS$_2$	Ti(NMe$_2$)$_4$¶ (heating at 150 °C) Bu^{t}SH# (57 °C) or Bu$_2^t$S$_2$** (115 °C)	Atmosphere at 300 ~ 600 °C	Thin film

*(NH$_4$)$_2$MoS$_4$: ammonium tetrathiomolybdate. †C$_8$H$_{18}$Se: di-tert-butylselenide. ‡C$_4$H$_{10}$Se: diethylselenide. §HS(CH$_2$)$_2$SH: 1,2-ethanedithiol. ‖V(NMe$_2$)$_4$: vanadium tetrakisdimethylamide. ¶Ti(NMe$_2$)$_4$: tetrakis(dimethylamido)titanium. #Bu^{t}SH: 2-methylpropanethiol. **Bu$_2^t$S$_2$: tert-butyldisulfide

(d)
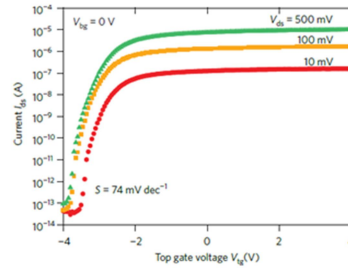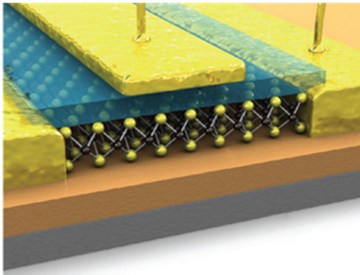
(e)
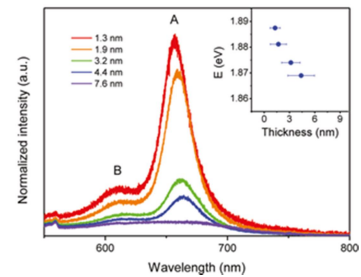

Figure 1-2-2 (a) Electronic properties of TMDs[20]. (b) Single-layer morphology of TMDs[20]. (c) Precursors and growth conditions of TMDs (CVD method)[20]. (d) Schematic illustration of top-gate monolayer MoS$_2$ FET device and its I$_{ds}$-V$_{ds}$ curve[22]. (e) Photoluminescence spectra of MoS$_2$ in each layer number[22]. TMDs' thickness can affect their electronic or optical properties.

Other kinds of interesting inorganic nanosheet materials are metal oxides and metal hydroxides. These nanosheets are obtained from their layered bulk metal oxides or hydroxides such as $Ti_{0.91}O_2$[23], MnO_2[24], $TiNbO_5$[25], RuO_2[26], and $Co(OH)_2$[27]. Their attractive electronic, magnetic, and optical functions can contribute to their utilization in many application such as capacitors, batteries, and dielectrics. There are two kinds of fabrication methods for this series of nanosheets. One is mechanical exfoliation of layered materials like graphene, and the other is chemical exfoliation. The counter ions in each interlayer can be changed to other guest bulky ions such as a tetrabutylammonium cation, and their interlayer distances increase to reduce interlayer electrostatic interaction, resulting in the exfoliation of the layers.
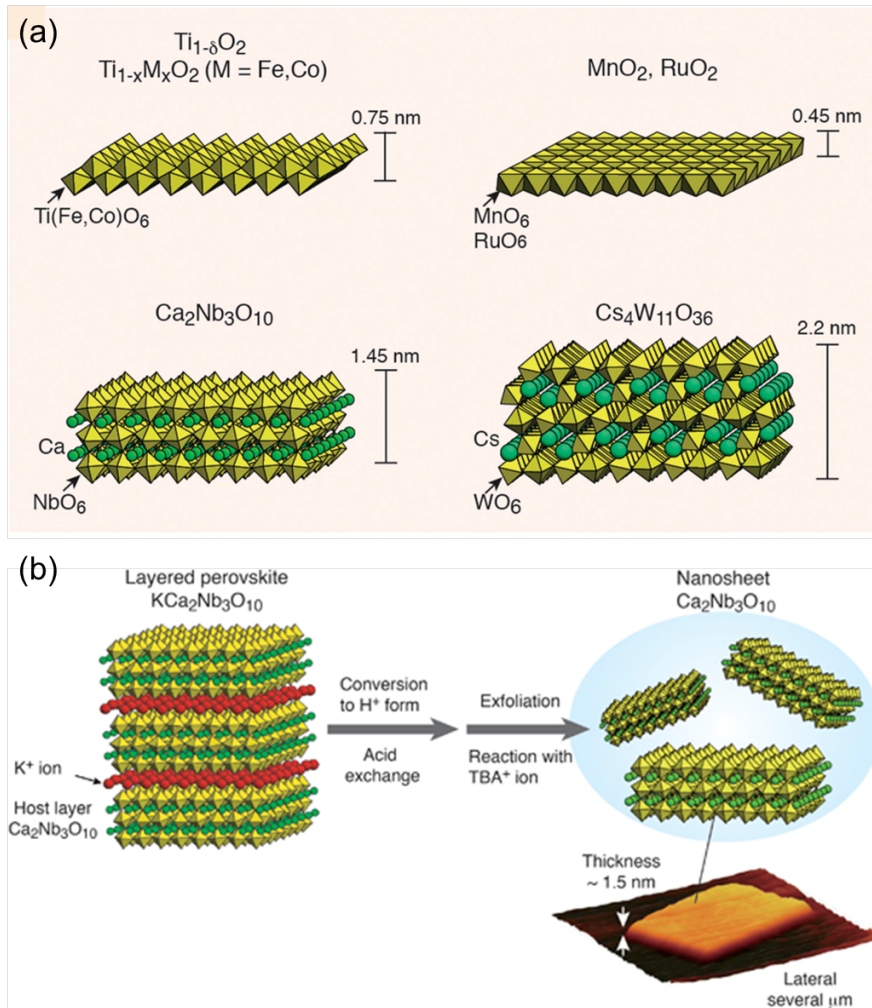

Figure 1-2-3 (a) Illustration of typical metal oxides[28]. (b) Illustration of chemical exfoliation method for metal oxides synthesis[28].

7

1-2-3 Surface covalent organic frameworks (SCOFs)

SCOFs are covalent organic frameworks (COF)s with atomically thickness. Different from the former examples, they are categorized as bottom-up nanosheets. More than two kinds of organic molecules react to link together and expand their network toward two-dimensional direction to fabricate atomically thin nanosheets. The organic molecular components are connected by covalent bonds which are stronger than hydrogen bonds or van der Waals interaction. The first SCOF material is reported in 2008[29] and its structure is confirmed by STM. Due to their well-defined molecular structure, recently there have been researches for various applications such as gas storage, catalysis, optoelectronics[30] or electronics[31].

(a)

BDBA   HHTP

29.8Å

50nm

(b)

HHTP

BDBA   BTBA   TBPA   BDBA   BPDA

COF-1   COF-6   COF-8   COF-5   COF-10
gra   bnn   bnn   bnn   bnn

Group 1   Group 2
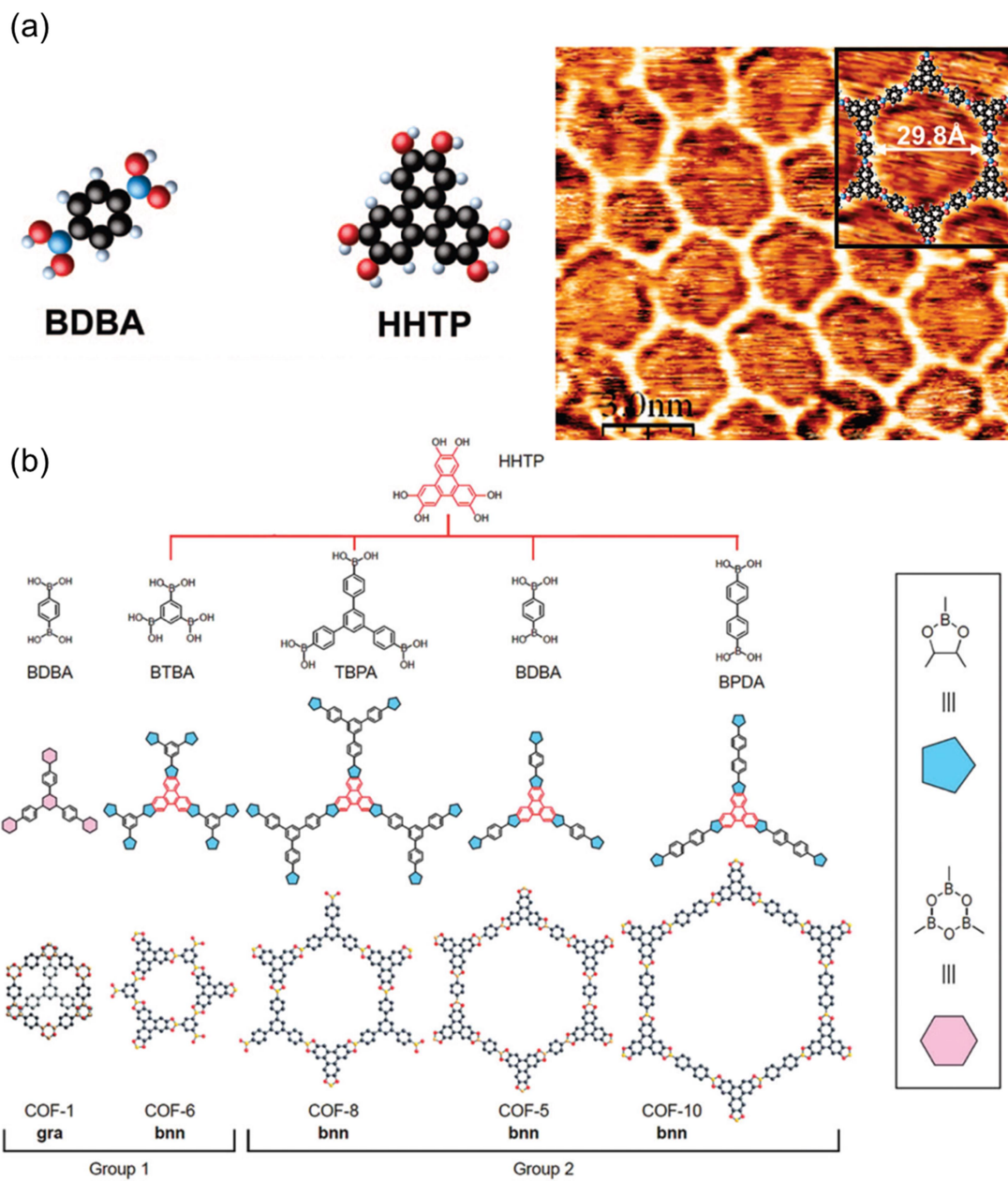
Figure 1-2-4 (a) The first SCOF composed of 1,4-benzenediboronic acid (BDBA) and 2,3,6,7,10,11-hexahydroxytriphenylene (HHTP)[29] and its STM image. (b) Illustration and chemical structure of SCOFs series[30].

9

1-3 Coordination nanosheets (CONASHs)

These days a new type of fascinating bottom-up nanosheets, coordination nanosheets (CONASHs), is emerging. CONASHs are composed of organic ligands and metal ions. Coordination bonds between the ligand and metal ions have good balance between bond strength and their reversibility so they are useful for constructing superstructure. Furthermore, broad diversities of the metal ions and organic ligands enable a large variety of functionalized materials.

The first CONASH synthesis was achieved by using a carboxylate-metal coordination bond[32] that is one of the most popular bonds in metal-organic frameworks (MOFs). Carboxylate ligands and iron(II) ions reacted in an ultra-high vacuum condition and deposited onto the Cu(100) substrate. STM revealed the expected two-dimensional nanosheet structure.

In contrast, recently CONASHs synthesized by wet processes have appeared. Compared to the dry process synthesis, special instruments are not required such as chemical vapor deposition equipment for nanosheets construction. It was first synthesized by using carboxyphenylporphyrin as a carboxylate ligand to create a two-dimensional MOF[33]. The Langmuir-Schäfer technique was used for nanosheet synthesis and the two-dimensional network was formed at the air/liquid interface by complexation. Similar Langmuir-Schäfer technique was also adopted in the case of the bis(terpyridine)metal complex motif[34].

Until now, most of CONASHs' researches have been focused on their synthesis and analysis of structure and morphology. However, the turning point of the CONASHs research came after the discovery of conductive functional bis(dithiolato)nickel nanosheet[35]. In this nanosheet simple liquid/liquid or gas/liquid interfacial synthesis produced multi-layer nanosheets (~1 μm thickness) and single-layer nanosheets (~0.6 nm thickness). The highly extended π-conjugated structure over the dithiolene rings of the nanosheets allows us to expect potential useful properties similar to graphene. Their fascinating properties were demonstrated by conductivity measurements; the electrical conductivity can be changed reversibly from 1.6×10^2 to 2.8 Scm^{-1} by tuning their oxidation state[36]. Thus, bis(dithiolato)nickel nanosheet can be used for electronic materials and it is the first functional CONASHs in which the components function is

introduced. Moreover, its single-layer is predicted as the first example of organic two-dimensional topological insulator[37] (insulator in its interior but conducting states at edge side), which is a promising electronic or spintronic material. Following the bis(dithiolato)nickel CONASH, other functional CONASHs have arose, such as other bis(dithiolato)metal nanosheets with electronic and electrocatalytic functions[38-40], bis(terpyridine)metal nanosheets with electrochromic devices[41], and bis(diimino)metal nanosheet[42,43] with super capacitors. The CONASHs research is now at the stage of exploring and expanding their functions. This promises great potential of the CONASHs as materials for applications.
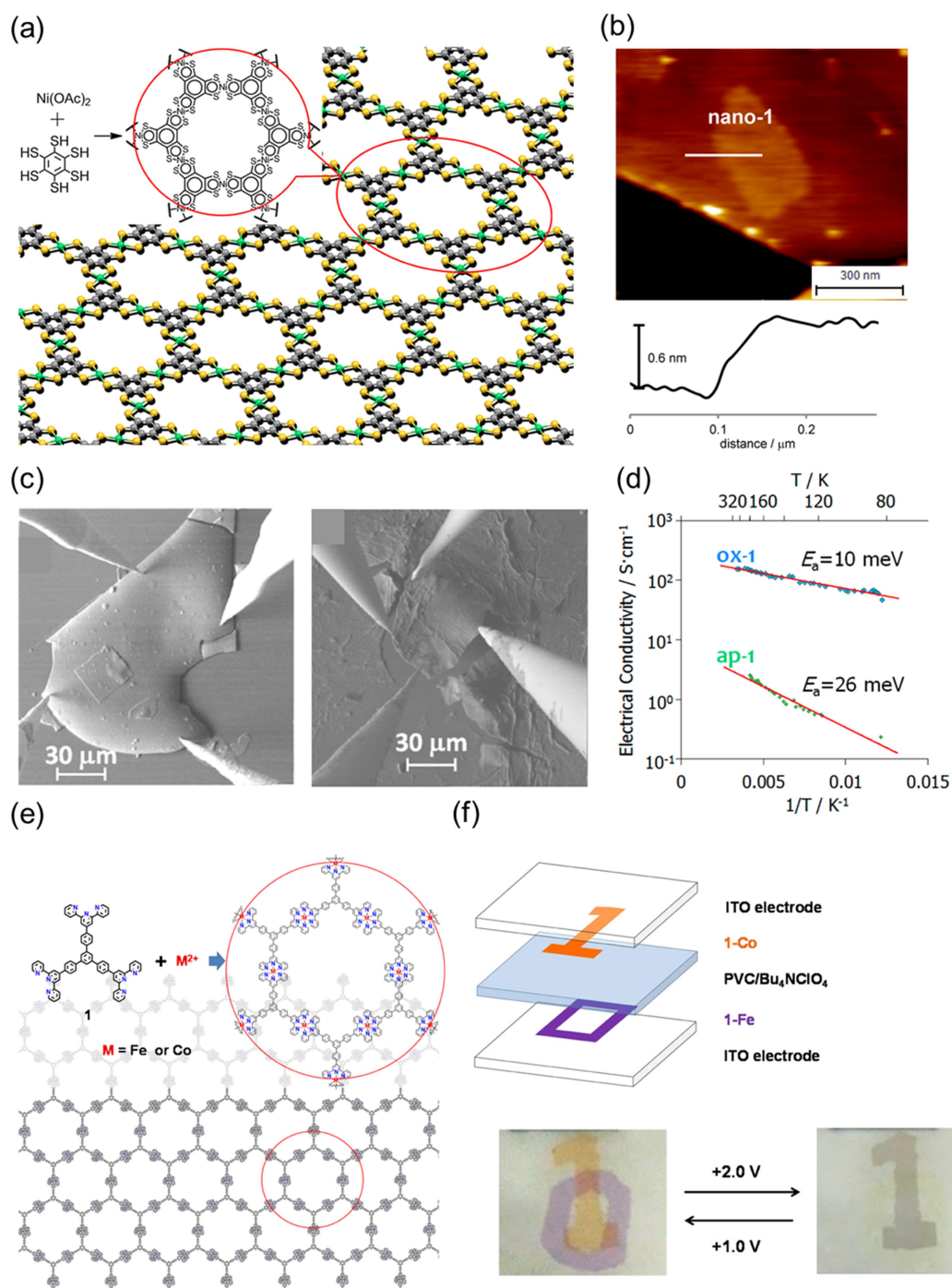
Figure 1-3-1 (a) Chemical structure of bis(dithiolato)nickel(II) nanosheet[35]. (b) AFM image of single-layer bis(dithiolato)nickel(II) nanosheet[35]. (c) Electrical conductivity measurements for bis(dithiolato)nickel(II) nanosheet under the control of SEM. (d) Conductivity-temperature dependence[36]. (e) Chemical structure of bis(terpyridine)metal nanosheet[38]. (f) Dual electrochromic device of bis(terpyridine)metal nanosheet[41].

1-4 The aim of this research

From the first research of the functional bis(dithiolene)metal CONASH, several new CONASHs' functions emerge as mentioned in the previous section. In considering CONASHs application, it is crucial to develop novel functionalities by selecting appropriate components, extending the scope of CONASHs

Therefore, in my Ph. D. research, I designed and demonstrated new functional bottom-up nanosheets by using various properties of metal complexes, with an aim to develope the CONASHs research toward application. This time I selected two kinds of new metal complex motifs as CONASHs components; one is bis(dipyrrinato)zinc and the other is bis(acetylacetonato)copper. The photoactive bis(dipyrrinato)zinc leads to fabricate photofunctional CONSASH, while the coordinatively unsaturated bis(acetylacetonato)copper produces a CONASH with molecular recognition.
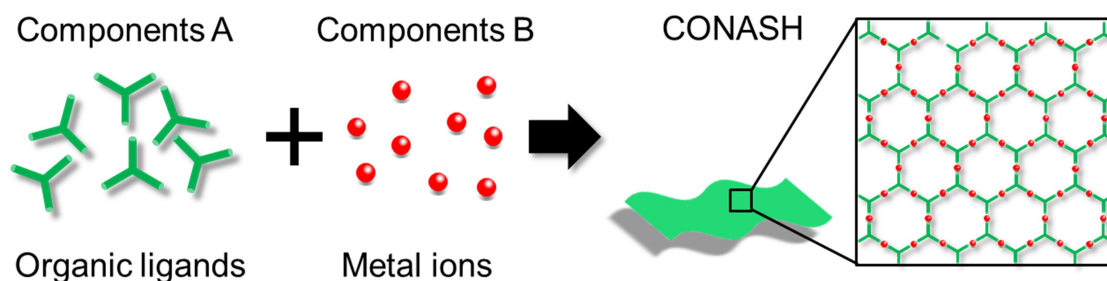

Figure 1-4-1 Schematic illustration of CONASH fabrication.

1-5 References

1) Novoselov, K. S.; Geim, A. K.; Morozov, S. V.; Jiang, D.; Zhang, Y.; Dubonos, S. V.; Grigorieva, I. V.; Firsov, A. A. *Science* **2004**, *306*, 666.

2) Fasolino, A.; Los, J. H.; Katsnelson, M. I. *Nat. Material* **2007**, *6*, 858-861.

3) Chen, J.-H.; Jang, C.; Xiao, S.; Ishigami, M.; Fuhrer, M. S. *Nat. Nanotech.* **2008**, *3*, 206-209.

4) Kuzmenko, A. B.; van Heumen, E.; Carbone, F.; van der Marel, D. *Phys. Rev. Lett.* **2008**, *100*, 117401-117404.

5) Novoselov, K. S.; Geim, A. K.; Morozov, S. V.; Jiang, D.; Katsnelson, M. I.; Grigorieva, I. V.; Dubonos, S. V.; Firsov, A. A. *Nature* **2005**, *438*, 197-200.

6) Chen, S.; Wu, Z.; Mishra, C.; Kang, J.; Zhang, H.; Cho, K.; Cai, W.; Balandin, A. A.; Ruoff, R. S. *Nat. Material* **2012**, *11*, 203-207.

7) Lee, C.; Wei, X.; Kysar, J. W.; Hone, J. *Science* **2008**, *321*, 385-388.

8) Son, Y.-W.; Cohen, M. L.; Louie, S. G. *Nature* **2006**, *444*, 347-349.

9) Bonaccorso, F.; Sun, Z.; Hasan, T.; Ferrari, A. C. *Nat. Photonics* **2010**, *4*, 611-622.

10) Stoller, M.D.; Park, S.; Zhu, Y.; An, J.; Ruoff, R. S. *Nano Lett.* **2008**, 8, 3498-3502.

11) Zhao, X.; Hayner, C. M.; Kung, M. C.; Kung, H. H. *Adv. Energy Mater.* **2011**, *1*, 1079-1084.

12) De Arco, L. G.; Ahang, Y.; Schlenker, C. W.; Ryu, K.; Thompson, M. E.; Zhou, C. *A.C.S. Nano* **2010**, *4,* 2865-2873.

13) Cohen-T. D.; Grossman, C. J. *Nano Lett.* **2012**, *12,* 3602-3608.

14) Yaokawa, R.; Ohsuna, T.; Morishita, T.; Hayasaka, Y.; Spencer, M. J. S.; Nakano, H. *Nat. Commun.* **2016**, *7*, 10657-10662

15) Roome, N. J.; Carey, J. D. *ACS Sppl. Mater. Interfaces* **2014**, *6*, 7743-7750.

16) Nigam, S.; Gupta, S.; Banyai, D.; Pandey, R.; Majumder C. *Phys. Chem. Chem. Phys.* **2015**, *17*, 6705-6712.

17) Favron, A.; Gaufrès, E.; Fossard, F.; P.-L'Heureux, A.-L.; Tang, N. Y.-W.; Lévesque, P. L.; Loiseau, A.; Leonelli, R.; Francoeur, S.; Martel, R.; *Nat. Mater.* **2015**, *14*, 826-832.

18) Mannix, A. J.; Zhou, X.-F.; Kiraly, B.; Wood, J. D.; Alducin, D.; Myers, B. D.; Liu, X.; Fisher, B. L.; Santiago, U.; Guest, J. R.; Yacaman, M. J.; Ponce, A.; Oganov, A. R.; Hersamm M. C.; Guisinger, N. P. *Sciecne* **2015**, *350*,

1513-1516.

19) Copper, D. R.; Anjou, B. D'.; Ghattamaneni, N.; Harack, B.; Hilke, M.; Horth, A.; Majlis, N.; Massicotte, M.; Vandsburger, L.; Whiteway, E.; Yu, V. *ISRN Condensed Matter Phys.* **2012**, *2012*, 1-56.

20) Manish, C.; Hyeon, S. S.; Goki, E.; Lain-Jong, L.; Kian, P. L.; Hua, Z.; *Nat. Chem.* **2013**, *5*, 263-275.

21) Mak, K. F.; Lee, C.; Hone, J.; Shan, J.; Heinz, T. F.; *Phys. Rev. Lett.* **2010**, *105*, 136805-136808.

22) Wang, Q. H.; Kalantar-Z., K.; Kis, A.; Coleman, J. N.; Strano, M. S. *Nature Nanotech.* **2012**, *7*, 699-712.

23) Sasaki, T.; Watanabe, M. *J. Phys. Chem. B* **1997**, *101*, 10159-10161.

24) Omomo, Y.; Sasaki, T.; Wang, L.; Watanabe, M. *J. Am. Chem. Soc.* **2003**, *125*, 3568-3575.

25) Akatsuka, K.; Takanashi, G.; Ebina, Y.; Haga, M.; Sasaki, T.; *J. Phys. Chem. C* **2012**, *116*, 12426-12433.

26) Sugimoto, W.; Iwata, H.; Yasunaga, Y.; Murakami, Y.; Takasu, Y. *Angew. Chem. Int. Ed.* **2003**, *42*, 4092-4096.

27) Ma, R.; Takada, K.; Fukuda, K.; Iyi, N.; Bando, Y.; Sasaki, T. *Angew. Chem. Int. Ed.* **2008**, *47*, 86-89.

28) Osada, M.; Sasaki, T. *Polymer J.* **2015**, *47*, 89-98.

29) Nikolas, A. A. Z.; Re´my, P.; Mathieu, A.; Daniel, C.; DidierG.; Denis, B.; Louis, P. *J. Am. Chem. Soc.* **2008**, *130*, 6678-6679.

30) Ding, S.-Y.; Wang, W. *Chem. Soc. Rev.* **2013**, *42*, 548-568.

31) Perepichka, D. F.; Rosei, F. *Science* **2009**, *323*, 216-217.

32) Dmitriev, A.; Spillmann, H.; Lin, N.; Barth, J. V.; Kern, K. *Angew. Chem. Int. Ed.*; **2003**, *42*, 2670-2673.

33) Makiura, R.; Motoyama, S.; Umemura, Y.; Yamanaka, H.; Sakata, O.; Kitagawa, H.; *Nature Mater.* **2010**, *9*, 565-571.

34) Bauer, T.; Aheng, Z.; Renn, A.; Enning, R.; Stemmer, A.; Sakamoto, J.; Shlüter, A. D. *Angew. Chem. Int. Ed.* **2011**, *50*, 7879-7884.

35) Kambe, T.; Sakamoto R.; Hoshiko, K.; Takada, K.; Ryu, J.-H.; Sasaki, S.; Kim, J.; Nakazato, K.; Takata, M.; Nishihara, H.; *J. Am. Chem. Soc.* **2013**, *135*, 2462-2465.

36) Kambe, T.; Sakamoto, R.; Kusamoto, T.; Pal, T.; Fukui, N.; Hoshiko, K.; Shimojima, T.; Wang, Z.; Hirahara, T.; Ishizaka, K.; Hasegawa S.; Liu, F.; Nishihara, H.; *J. Am. Chem. Soc.* **2014**, *136*, 14357-14360.

37) Wang, Z. F.; Su, N.; Liu, F. *Nano Lett.* **2013**, *13*, 2842-2845.

38) Pal, T.; Kambe, T.; Kusamoto, T.; Foo, M. L.; Matsuoka, R.; Sakamoto, R.; Nishihara, H. *ChemPlusChem*, **2015**, *80*, 1255-1258.

39) Huang, X.; Sheng, P.; Tu, Z.; Zhang, F.; Wang, J.; Geng, H.; Zou, Y.; Di, C.-an; Yi, Y.; Sun, Y.; Xu, W.; Zhu, D.; *Nat. Commun.* **2015**, *6*, 7408-7415. ,

40) Dong, R.; Pfeffermann, M.; Liang. H.; Zheng, Z.; Zhu, X.; Zhang, J.; Feng, X. *Angew. Chem. Int. Ed.* **2015**, *54*, 12058-12063.

41) Takada, K.; Sakamoto, R.; Yi, S.-T.; Katagiri, S.; Kambe, T.; Nishihara, H. *J. Am. Chem. Soc.* **2015**, *137*, 4681-4689.

42) Campbell, M. G.; Sheberla, D.; Liu, S. F.; Swager, T. M.; Dincä, M. *Angew. Chem. Int. Ed.* **2015**, *54*, 4349-4352

43) Sheberia, D.; Bachman, J. C.; Elias, J. S.; Sun, C.-J.; S.-Horn, Y.; Dincä, M. *Nat. Mater.* **2016**, doi:10.1038/nmat4766.

Chapter 2

Bis(dipyrrinato)zinc(II) nanosheet

2-1 Introduction

2-1-1 Bis(dipyrrinato)zinc(II) complexes

Dipyrrin is a planar organic molecule with two pyrrole rings linked by a methine group. Its π-conjugation causes dipyrrin's strong visible light absorption through π-π^* transition. One of the most attractive dipyrrin complexes is 4,4-difluoro-4-bora-3a,4a-diaza-s-indacenes, that is BODIPYs[1], which show small Stoke shift (around 500 cm^{-1}) and intense fluorescence. The flexible modifiability of the dipyrrin unit exhibits tunable optical properties (such as fluorescent wavelength) and it enables BODIPYs to be utilized in luminescent probes or dyes.

In the case of dipyrrinatometal complexes, they were reported as suitable materials for supramolecules[2], coordination polymers[2,3], and metal organic frameworks (MOFs)[2,4]. The spontaneous and reversible coordination reaction makes them suitable for these components. Their fascinating photofunction was also studied to achieve intense light absorption, enhanced tunable luminescence and high quantum yield by appropriate ligand selection[5].
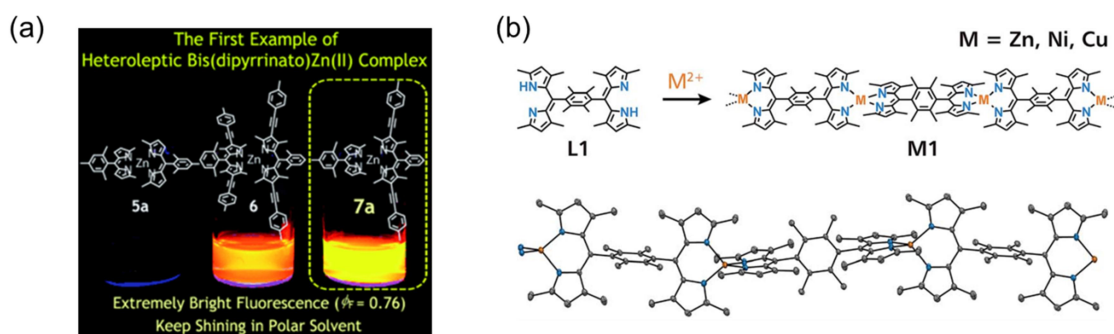

Figure 2-1-1 (a) Mononuclear Bis(dipyrrinato)zinc(II) complex with extremely strong fluorescence[5]. (b) Chemical structure and ORTEP drawing of one-dimensional bis(dipyrrinato)zinc(II) wire with the probability of 50%[3].

2-1-2 The aim of this study

  In consideration of its attractive photofunctional features, I selected bis(dipyrrinato)zinc(II) as a component of a new functional CONASH. The present work describes a bis(dipyrrinato)zinc(II) nanosheet, **N1** (**multi-layer N1**, **single-layer N1**, and **several-layer N1**) synthesized from a three-way dipyrrin ligand (1,3,5-tris-[4'-(5-mehyl-1H-pyrrole-2-yl(5-methyl -2H-pyrrole-2-ylidene)methyl)phenyl]benzene, **L1**) and zinc acetate. Coordination reaction of dipyrrin ligands with metal ions in the reversible and mild condition promises bis(dipyrrinato)zinc to be suitable building blocks for bottom-up nanosheets. This character may contribute the nanosheets to form single layer with large flat homogenous area, which is necessary for application but not achieved in previous bottom-up CONASHs. The bis(dipyrrinato)zinc motif can act not only as a connecting point but also as a photofunctional moiety because of its attractive optical properties as mentioned above. Therefore, in this study I have tackled with two challenges; one is to fabricate huge homogeneous area of CONASH for considering utilization in application, and the other is to achieve introduction of the bis(dipyrrinato)zinc(II) complex's attractive photofunction to the nanosheet. Actually, this is the first example of introducing photofunctionality to CONASHs, and it will lead to expand their utilities and functions for application.
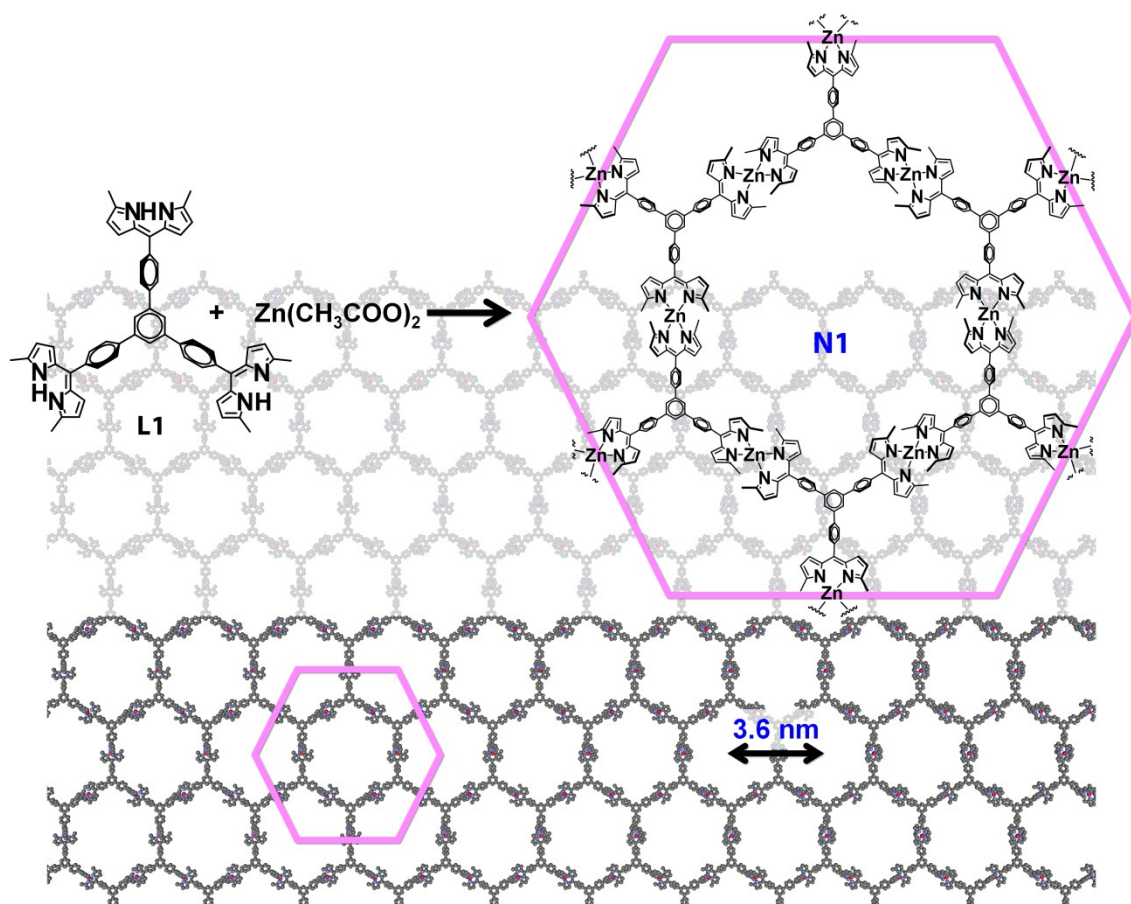
Figure 2-1-2 Bis(dipyrrinato)zinc(II) nanosheet (**N1**): CONASH of the present work and chemical structure of the three-way dipyrrin ligand **L1**[6].

2-2 Experimental section

Materials.

5'-(4-Formylphenyl)-[1,1':3',1"-terphenyl]-4,4"-dicarbaldehyde[7], 2-methylpyrrole[8], 2-((3,5-dimethyl-2H-pyrrol-2-ylidene)(2,6-dimethylphenyl)methyl)-3,5-dimethyl-1H-pyrrole[9] and 2-methyl-5-((5-methyl-2H-pyrrol-2-ylidene)(phenyl) methyl)-1H-pyrrole[10] were synthesized according to previous reports. Dichloromethane, acetonitrile and ethanol for the interfacial synthesis of the **N1**, pretreatments of substrates, washing substrates and photoelectric conversion were supplied from Kanto Chemical Co., Inc. as high-performance liquid chromatography grade and were used without further purification. Water was purified using a Milli-Q purification system (Merck KGaA). Tetra-n-butylammonium perchlorate as a supporting electrolyte was purified by recrystallization from ethanol, which was dried in vacuo. Solvents for organic syntheses were purified using a solvent purification system (Ultimate Solvent System, Nikko Hansen & Co., Ltd). The other chemicals were general grades and were used as received. All procedures were conducted under an ambient condition otherwise stated.

Apparatus for the identification of molecular compounds.

^{1}H (500 or 400 MHz) and ^{13}C (125 or 100 MHz) nuclear magnetic resonance (NMR) spectra were recorded on a Bruker-DRX500, JEOL ECX-400 or JEOL AL-400 spectrometer. Fast atom bombardment mass spectrometry (FAB-MS) and electrospray ionization time-of-flight spectrometry were conducted using a JEOL JMS-700 MStation and Micromass LCT Premier XE mass spectrometer, respectively.

Synthesis of L1.

5'-(4-Formylphenyl)-[1,1':3',1"-terphenyl]-4,4"-dicarbaldehyde (450 mg, 1.2 mmol) and 2-methylpyrrole (0.63 ml, 7.5 mmol) were dissolved in dichloromethane (100 ml) under a nitrogen atmosphere. One drop of trifluoroacetic acid was added, and the solution changed from light yellow to bright red and was stirred at room temperature for 3 h. When complete consumption of the aldehyde was confirmed by thin-layer chromatography, a solution of chloranil (848 mg, 3.4 mmol) in dichloromethane was added, and the resultant mixture was stirred for an additional 15 min. The reaction

mixture was washed with water, dried over magnesium sulfate, filtered and evaporated. The crude product was purified by column chromatography on aluminum oxide (activity II–III) with dichloromethane as an eluent to yield a deep-yellow powder (231 mg, 25%).

^{1}HNMR (400 MHz, CDCl$_3$): δ 7.95 (s, 3H), 7.80 (d, J=8.0 Hz, 6H), 7.61 (d, J=8.0 Hz, 6H), 6.56 (d, J=4.0 Hz, 6H), 6.19 (d, J=4.0 Hz, 6H), 2.47 (s, 18H); 13C NMR (100 MHz, CDCl$_3$): δ 165.18, 146.78, 141.99, 137.88, 135.32, 132.12, 130.51, 128.89, 127.12, 116.54, 112.11, 105.97 and 18.21; HR-FAB-MS (m/z): [M]$^+$ calculated for C$_{57}$H$_{48}$N$_6$, 816.3940; found, 816.3924.

Synthesis of multi-layer N1.

A 50-ml cylindrical glass vial (4.0 cm in diameter) was used as the reaction container. **L1** was dissolved in dichloromethane to a concentration of 1.0×10^{-4} mol/L, and 10 ml of the solution was poured into the vial. Then, pure water (10 ml) was layered gently onto the organic phase, which served as a buffer layer. After 2 h, aqueous zinc acetate solution (0.1 mol/L 10 ml) was slowly added to the buffer layer. The reaction system was left undisturbed for 4 days to obtain an orange film at the liquid/liquid interface. The resulting **multi-layer N1** could be deposited on various substrates.

Synthesis of single-layer N1 or several-layer N1.

A 50-ml glass vial (4.0 cm in diameter) was used as the reaction container. Aqueous zinc acetate (0.05 mol/L, 30 ml) was poured into the vial. A small amount of mixture solution (dichloromethane: ethyl acetate =14: 1) of **L1** was then sprinkled gently on the surface of the aqueous phase: **single-layer N1** was synthesized using 5.0 μl of **L1** solution (7.4×10^{-5} mol/L), whereas 20 μl of **L1** solution (7.4×10^{-5} mol/L) was used for the several-layer nanosheet. After spontaneous evaporation of the organic solvent, the reaction system was left undisturbed, such that **N1** was produced at the air/liquid interface. **Single-layer** or **several-layer N1** was then transferred onto substrates using the Langmuir–Schäfer method.

Synthesis of mononuclear bis(dipyrrinato)zinc(II) complex M1.

Zinc acetate dihydrate (36.7 mg, 0.17 mol) and triethylamine (0.11 ml) were added to a dichloromethane solution (20 ml) of 2-((3,5-dimethyl-2H-pyrrol-2-ylidene)(2,6-dimethylphenyl)methyl)-3,5-dimethyl

-1H-pyrrole (122 mg, 0.40 mmol), and the reaction mixture was stirred overnight at room temperature. Methanol (20 ml) was added to recrystallize the product as an orange solid (60.5 mg, 45%).

^{1}H NMR (500 MHz, CDCl$_3$): δ 7.21 (t, J=7.6 Hz, 2H), 7.11 (d, J=7.6 Hz, 4H), 5.91 (s, 4H), 2.16 (s, 12H), 2.04 (s, 12H) and 1.28 (s, 12H); ^{13}C NMR (125 MHz, CDCl$_3$): δ 156.07, 143.26, 143.06, 139.18, 135.95, 134.27, 127.98, 127.88, 119.74, 19.33, 16.13 and 14.70; HR-FAB-MS (m/z): [M]$^+$ calculated for C$_{42}$H$_{46}$N$_4$Zn, 670.3014; found, 670.3011.

Synthesis of mononuclear bis(dipyrrinato)zinc(II) complex M2.

A solution of 2-methyl-5-((5-methyl-2H-pyrrol-2-ylidene)(phenyl)methyl)-1H-pyrrole (450 mg, 1.8 mmol) in methanol (10 ml) was poured into a suspension of anhydrous zinc acetate (168 mg, 0.92 mmol) in methanol (3 ml). The mixture was stirred overnight at room temperature. The reaction mixture was filtered, and the resultant solid was washed with methanol. Filtration yielded a light orange solid (463 mg, 90%).

^{1}H NMR (400 MHz, CDCl$_3$): δ 7.50-7.39 (m, 10H), 6.55 (d, J=4.0 Hz, 2H), 6.18 (d, J=4.0 Hz, 2H) and 2.12 (s, 12H); 13C NMR (100MHz, CDCl3): δ 159.44, 144.71, 139.52, 139.39, 133.22, 130.89, 128.17, 127.14, 117.10 and 16.62; HR-FAB-MS (m/z): [M]$^+$ calculated for C$_{42}$H$_{46}$N$_4$Zn, 558.1762; found, 558.1782.

Synthesis of a precursor for M3.

To a dichloromethane (20 ml) solution of ethyl 3-(4-formylphenyl)propanoate (618 mg, 3.0 mmol) and 2-methylpyrrole (0.55 ml, 6.3 mmol), trifluoroacetic acid (10 ml) was added, under a nitrogen atmosphere, and the solution was stirred overnight at room temperature. Chloranil (749 mg, 3.0 mmol) was added and stirred for another 30 min. After evaporation of the solvent, the residue was passed through a short pad of aluminum oxide (activity II–III) using dichloromethane as an eluent. After evaporation of the solvent, the crude product was purified by column chromatography on aluminum oxide (activity II–III) with hexane/dichloromethane (1:1 v/v) as an eluent. The yellow band was collected and evaporated to yield ethyl 3-(4-((5-methyl-1H-pyrrol-2-yl)(5-methyl-2H-pyrrol-2-ylidene)methyl)phenyl) propanoate as an orange oil (146 mg, 14%).

^{1}H NMR (500 MHz, CDCl3) δ 7.41 (d, J=8.2 Hz, 2H), 7.26 (d, J=8.2 Hz, 2H), 6.48 (d, J=3.8 Hz, 2H), 6.17 (d, J=3.8 Hz, 2H), 4.18 (q, J=7.3 Hz, 2H), 3.05 (t, J=7.9 Hz, 2H), 2.71 (t, J=7.9 Hz, 2H), 2.46 (s, 6H) and 1.28 (t, J=7.3 Hz, 3H); 13C NMR (125 MHz, CDCl3) δ 172.84, 153.67, 140.99, 139.91, 138.30, 135.49, 130.99, 128.96, 127.41, 117.35, 60.49, 35.81, 30.79, 16.29 and 14.27; HR-FAB-MS (m/z): $[M]^+$ calculated for $C_{22}H_{24}N_2O_2$, 348.1829; found, 348.1838.

Synthesis of M3.

Ethyl 3-(4-((5-methyl-1H-pyrrol-2-yl)(5-methyl-2H-pyrrol-2-ylidene)methyl) phenyl)propanoate (100 mg, 0.29 mmol) was added to tetrahydrofuran (30 ml) and water (5 ml), and the mixture was stirred at room temperature for 5min. Then, an aqueous solution (10 ml) of NaOH (115 mg, 2.9 mmol) was added, and the reaction mixture was stirred overnight at room temperature. After adjusting the pH of the reaction mixture to 4 using aqueous hydrochloric acid (1.0×10^{-4} mol/L), the mixture was poured into water (50 ml) and washed with ether (20 ml×3). The water layer was then treated with a solution of anhydrous zinc acetate (58 mg, 0.29 mmol) in water (3 ml). The mixture was extracted with dichloromethane and dried over sodium sulfate. The solvent was evaporated under a reduced pressure to yield a dark orange solid of **M3** (3.0 mg, 3%).

^{1}H NMR (500 MHz, dimethylsulfoxide-d_6): δ 12.34 (bs, 2H), 7.34–7.30 (m, 8H), 6.33 (d, J=4.0 Hz, 4H), 6.20 (d, J=4.0 Hz, 4H), 2.91 (t, J=7.6 Hz, 4H), 2.61 (t, J=7.6 Hz, 4H) and 2.39 (s, 12H); 13C NMR (125 MHz, CDCl3) δ 158.99, 144.79, 139.06, 133.29, 130.90, 130.59, 127.60, 117.85, 31.16, 25.62 and 16.49 (two quaternary carbons are missing because of low solubility or overlaps with other peaks); HR-ESI-MS (m/z): $[M-H^+]$ calculated for $C_{40}H_{37}N_4O_4Zn$, 701.2106; found, 701.2122.

Pretreatments for substrates.

HOPG was cleaved with a piece of cellophane tape to obtain a flat and clean surface just before use. Si(111) substrates were hydrophobized using 1,1,1,3,3,3-hexamythyldisilazane (HMDS). The procedure to form a HMDS/Si(111) surface is as follows. The Si(111) substrate covered with a natural SiO_2 layer was immersed in an ethanol solution of HMDS (1 v/v%) for 1 day. The substrate was then washed with ethanol several times before

being annealed at 130°C for 30 min. ITO (on glass), quartz and SnO_2 (on ITO-covered glass, $5\Omega sq^{-1}$) substrates were sonicated in acetone (10 min×2), water (10 min×2) and nonionic detergent in water (30 min). Then, the substrate was washed with water until the bubbles of the detergent disappeared before being sonicated in water (10 min×3) and ethanol (10 min×2). The cleaned substrate was stored in water, and dried by nitrogen blow just before use.

Layering of single-layer N1 (stacked single-layer N1).

A Langmuir–Blodgett trough (KSV 2000, KSV NIMA) was used as a reaction container. Before a zinc acetate aqueous solution (0.05 mol/L) was poured into the trough as a subphase, the trough was washed with ethanol and water. The surface of the aqueous solution was cleaned by suctioning the surface of the subphase several times on compressing the trough barrier. Then, a dichloromethane solution of **L1** ($7.4×10^{-5}$ mol/L, 27.7 µl) was dropped gently onto the surface of the subphase. Under this condition, the ideal coverage of **single-layer N1** reached 90% of the trough area. After spontaneous evaporation of the organic solvent, the reaction system was left undisturbed for 4 h, such that **single-layer N1** was produced at the air/liquid interface. The trough was then compressed to yield a trough area of 69.8 cm2 (90% of the initial trough area) at a surface pressure of 0.04 mN/m. Under these conditions, **single-layer N1** was transferred onto a quartz substrate via the Langmuir–Schäfer method. The trough was then shrunk by the same area as the substrate, and the next transfer was conducted. This process was repeated to layer **single-layer N1** (stacked **single-layer N1**).

Guest inclusion.

Multi-layer N1 (thickness: 700 nm) was deposited on a quartz or ITO substrate. The modified substrate was immersed in a dichloromethane solution of Rhodamine B ($5.0×10^{-5}$ mol/L) for 15 h and was then rinsed with dichloromethane to yield Rhodamine B-encapsulated multi-layer **N1**.

Analyses for N1.

XPS was conducted using a PHI 5000 VersaProbe (Ulvac-Phi, Inc.). Al $K\alpha$ (15 kV, 25W) was used as the X-ray source, and the beam was focused on a $100\text{-}mm^2$ area. The spectra were analysed with MultiPak Software and

standardized using the C 1s peak at 284.6 eV. AFM and STM were performed using an Agilent Technologies 5,500 scanning probe microscope under an ambient condition. AFM was performed in high-amplitude mode (tapping mode) with a silicon cantilever PPP-NCL (Nano World). The probe for STM (Pt-Ir alloy, 4:1, 0.25mm in diameter) was cut from a wire using a nipper to obtain a sharp edge. An optical microscope image was taken using a VHX-100 (Keyence Corporation). A field emission scanning electron microscopic image was collected using a JEOL JSM-7400FNT. Transmission electron microscopy images/SAED patterns were recorded at accelerating voltage of 75 kV using a Hitachi HF-2000 equipped with an AMTCCD camera. The sample was prepared by depositing **multi-layer N1** (thickness: 700 nm) on a carbon film supported by a copper grid (ELS-C10, stem Co., Ltd) directly from the liquid/liquid interface. To acquire electron diffractions, I focused on the edge of **multi-layer N1**. To reproduce the obtained SAED pattern, three-dimensional structures of **multi-layer N1**, which comprise piles of **single-layer N1**, were considered. Here I treated AA-, AB- and ABC-stack models, which are often encountered in layered materials. The three-dimensional lattice was optimized at the molecular mechanics level of theory with the UFF VALBOND 1.1 force field on an Accelrys Cerius2 ver3.1 program package. The unit cell was assumed to be trigonal such that the α, β, and γ angles were constrained to be 90, 90, and 120, respectively. First, I performed a calculation on the AA-stacking structure with its molecular geometries and cell lengths being fully optimized. Initial structures for the AB- and ABC-stack models were constructed from the optimized AA-stack one by giving parallel displacement to the B and/or C layers. The SAED patterns were simulated by implementing CrystalMaker 2.6.3 and SingleCrystal 2.3 (CrystalMaker Software Ltd). UV/vis absorption spectra were recorded on a JASCO V-570 spectrometer in transmission mode. A quartz or SnO_2 substrate modified with **N1** was set vertical to the probe light. Fluorescence and excitation spectra were recorded on a HITACHI F-4500 fluorospectrometer.

Photoelectric conversion.

  N1 with thicknesses <155 layers was deposited on a transparent SnO_2 electrode using the repeated Langmuir–Schäfer procedure shown in Figure 2-13-2 (b),(c). On the other hand, **N1** with thicknesses of >155 layers was

fabricated directly using the liquid/liquid interfacial synthesis (Figure 2-3-1) and deposited on the electrode. Before photoelectric conversion, each **N1** physisorbed on a transparent SnO_2 electrode was always subjected to UV/vis spectroscopy, acquiring spectra from four different positions. This series of measurements allowed us to ensure the uniformity of **N1** and to quantify the thickness of **N1** using the average absorbance at 500nm and that of **single-layer N1** (0.00101 from the slope of Figure 2-13-2(c)). The average absorbance at 500nm was also used in calculating the

quantum yield of photoelectric conversion (vide infra). The modified SnO_2 electrode was used as a working electrode (photoanode). Silver and platinum wires were employed as reference and counter electrodes, respectively. The resulting three-electrode system was immersed in a homemade photoelectrochemical cell (Figure 2-13-4 (a)), which was filled with an acetonitrile solution of tetra-nbutylammonium perchlorate (0.1 mol/L) containing TEOA (0.05 mol/L) as a sacrificial donor reagent. The cell was sealed and deoxygenized by argon bubbling for 30 min. Monochromatic light for the action spectrum shown in Figure 2-13-6(a) (400–600 nm in every 20 nm) was extracted from a xenon lamp (MAX–302, Asahi Spectra Co., Ltd), the photon flux of which was monochromated by a monochromator (CT-10, JASCO Corporation). For the other experiments, 500-nm light was used exclusively, which was provided by the xenon lamp equipped with a band-pass filter. The active area of the electrode was 0.264 cm^2, which was determined by a fluorocarbon rubber o-ring. The electrode potential and photocurrent acquisition of the photoelectric conversion system were controlled using an electrochemical analyser (ALS 750A, BAS Inc.). The photoanode was fixed at 0.0 V versus the silver reference electrode for the data shown in Figure 2-13-4, 2-13-5, 2-13-6 and 0.15 V for the other data, including those for **M2** and **M3**. At both potentials, no anodic current induced by the direct oxidation of TEOA in the dark was observed. The quantum yield of photoelectric conversion, ϕ, was calculated using equation (1):

$$\phi = n_e/n_p$$

where n_e is the mole of electrons that flows in the circuit per unit time (in mol/s) and n_p is the mole of photons absorbed by the sensitizer per unit time (in mol/s). n_e and n_p were calculated using equations (2) and (3):

$$n_e = i/F$$

$$n_p = W\lambda[1\text{-}10^{-A}]/N_A hc$$

where i is the current flow (in A), F is the Faraday constant (9.65×10^4 C/mol), W is the photon flux of incident light (in J/s), λ is the wavelength of the irradiated light (5.00×10^{-7} m), A is the absorbance at the irradiated wavelength, N_A is the Avogadro constant (6.02×10^{23} mol/L), h is the Planck constant (6.63×10^{34} Js) and c is the velocity of light (3.00×10^8 m/s). i was calculated using equation (4):

$$i = i_L \text{-} i_D$$

where i_L is the average light current for the first cycle (10 s) and i_D is the average dark current just before the illumination of light. A photon counter (8230E and 82311B, ADC Corporation) was employed for the quantification of W. For every sample, W was measured independently. A typical value for W was ~0.20 mW. When i was below the measurable level (<1.0 nA), W was increased to 1.0–2.0 mW such that the photocurrent signal was amplified. For referential mononuclear complex **M2**, film formation was conducted as follows: two droplets from a disposable Pasteur pipette of an acetonitrile solution of **M2** (1.86×10^{-5} mol l/L) were dripped onto a SnO_2 substrate (~0.8 cm^2). The substrate was then dried under vacuum for 10 min to allow the solvent to evaporate. The modified SnO_2 electrode was subjected to photoelectric conversion, following the procedure for **N1** except that aqueous 0.1 mol l/L sodium sulfate was used as an electrolyte solution; this change prevented the **M2** film from redissolution. Referential mononuclear complex **M3** was immobilized on a SnO_2 electrode through the carboxy group using the self-assembled monolayer procedure[11]. A SnO_2 substrate was immersed in a dimethylsulfoxide solution of **M3** (1.96×10^{-3} mol/L) for 1 day at room temperature, and the decorated substrate was rinsed with dimethylsulfoxide and dried by an argon blow. The modified SnO_2 electrode was subjected to photoelectric conversion using the same procedure as **N1**.

2-3 Fabrication of multi-layer N1

Multi-layer film of a bis(dipyrrinato)zinc(II) nanosheets (**multi-layer N1**) were prepared through liquid/liquid interfacial synthesis. In this method unmixed two solvents were used to make interface, so that the complexation reaction of **L1** and zinc ions could be limited toward two-dimensional interfacial direction. Connection and expansion of the bis(dipyrrinato)zinc(II) complex moieties at the interface led to construction of the two-dimensional nanosheets.

In this case, I employed an interface between dichloromethane and water for the complexation reaction field. At first I added 10 mL dichloromethane solution of **L1** (10^{-4} mol/L) to a 50-mL glass vial (4.0 cm in diameter) and then 10 mL of pure water was set gently on the dichloromethane solution. It was kept calm for 2 hours after the process in order to stabilize the interface. After that, I slowly added 10 mL aqueous solution of zinc acetate (0.1 mol/L) without making any shock to the vial. The final concentration of zinc acetate was 0.05 mol/L. The interface was kept calm for 4 days to grow the nanosheets gradually and finally orange film of **multi-layer N1** was produced at the interface.

(a) ... Water 10 mL ... Zn(OAc)$_2$/ water 50 mM 20 mL

2h

1.0×10^{-4} mol/L
10 mL
(CH$_2$Cl$_2$)

L1

(b) Zn(OAc)$_2$ aq.

Multi-layer N1

L1 (CH$_2$Cl$_2$)
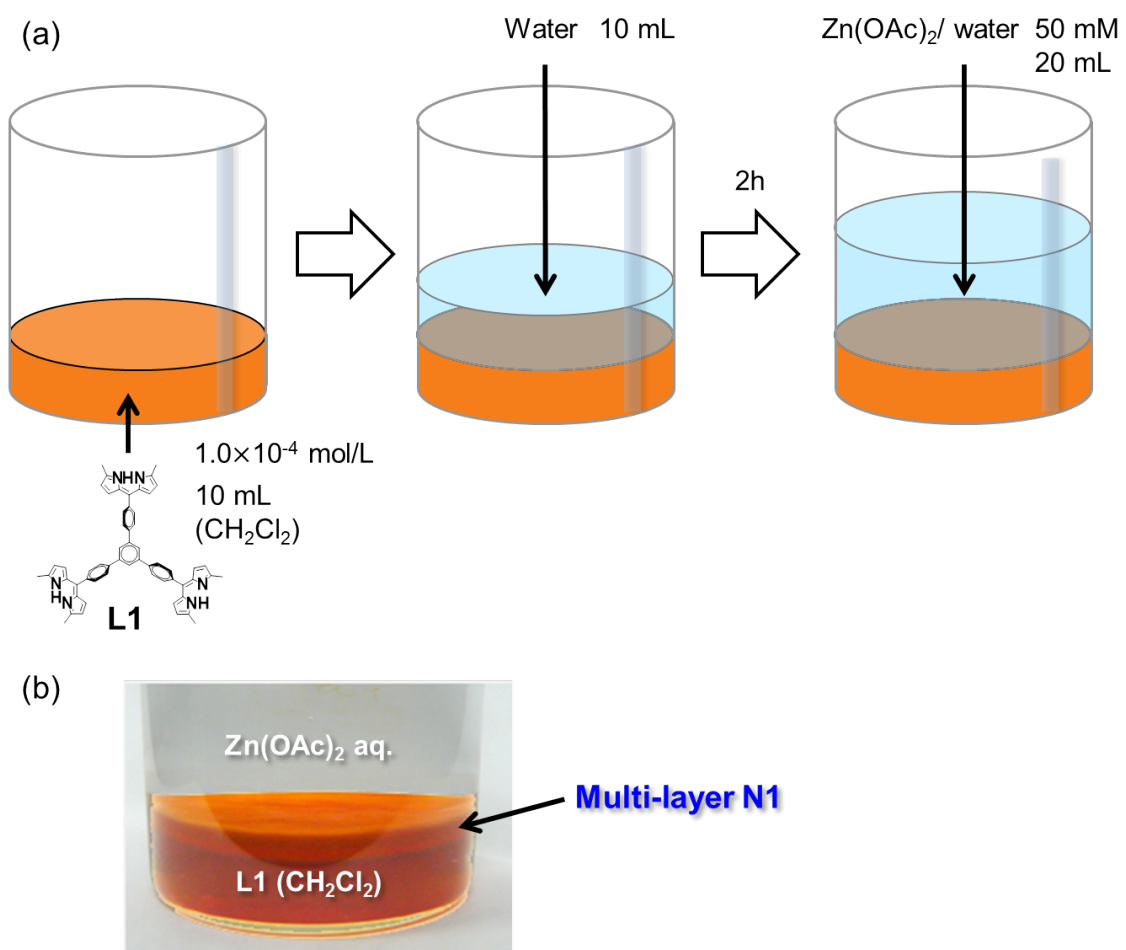
Figure 2-3-1 (a) Schematic illustration of liquid/liquid interfacial synthesis of **multi-layer N1**.
(b) Photograph of **multi-layer N1** at the interface produced by liquid/liquid interfacial synthesis.

Subsequently, top aqueous layer of zinc acetate was almost removed and left about 5 mL to avoid the film to be broken. About 2 mL of pure water was added gently, and the same amount of zinc ion solution was removed. This cycle was repeated more than 10 times in order to dilute the aqueous layer. Then the bottom organic layer was also diluted by the same way. After dilution of both layers, almost 20 mL of pure water was added to the aqueous layer and nearly 8 mL ethanol was added to the aqueous layer to form three layers in the vial (dichloromethane, water, and ethanol layers). The middle water layer was then removed totally. At next, about 5 mL of the lower dichloromethane solution was removed and 5 mL of ethanol was added to the lower layer. After conducting this cycle for several times, the **multi-layer N1** could float in the ethanol single phase. Finally the floating **multi-layer N1** could be scooped onto several substrates such as HOPG, HMDS/Si(111), ITO, quartz, and SnO_2. The deposited **multi-layer N1** was rinsed by pure water, ethanol, and dichloromethane to remove metal ions and organic ligand. Actually, the **multi-layer N1** could not be dissolved in any common solvents such as water, MeOH, EtOH, CH_2Cl_2, $CHCl_3$, DMF, DMSO, and CH_3CN, which suggests the polymer structure of **multi-layer N1**.
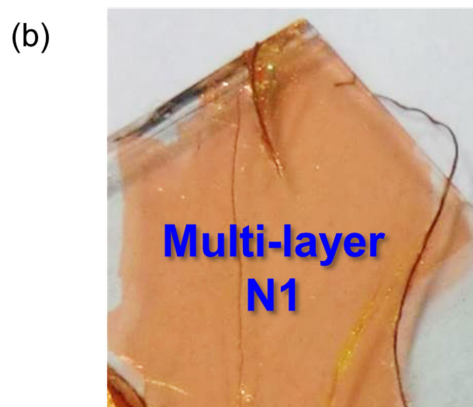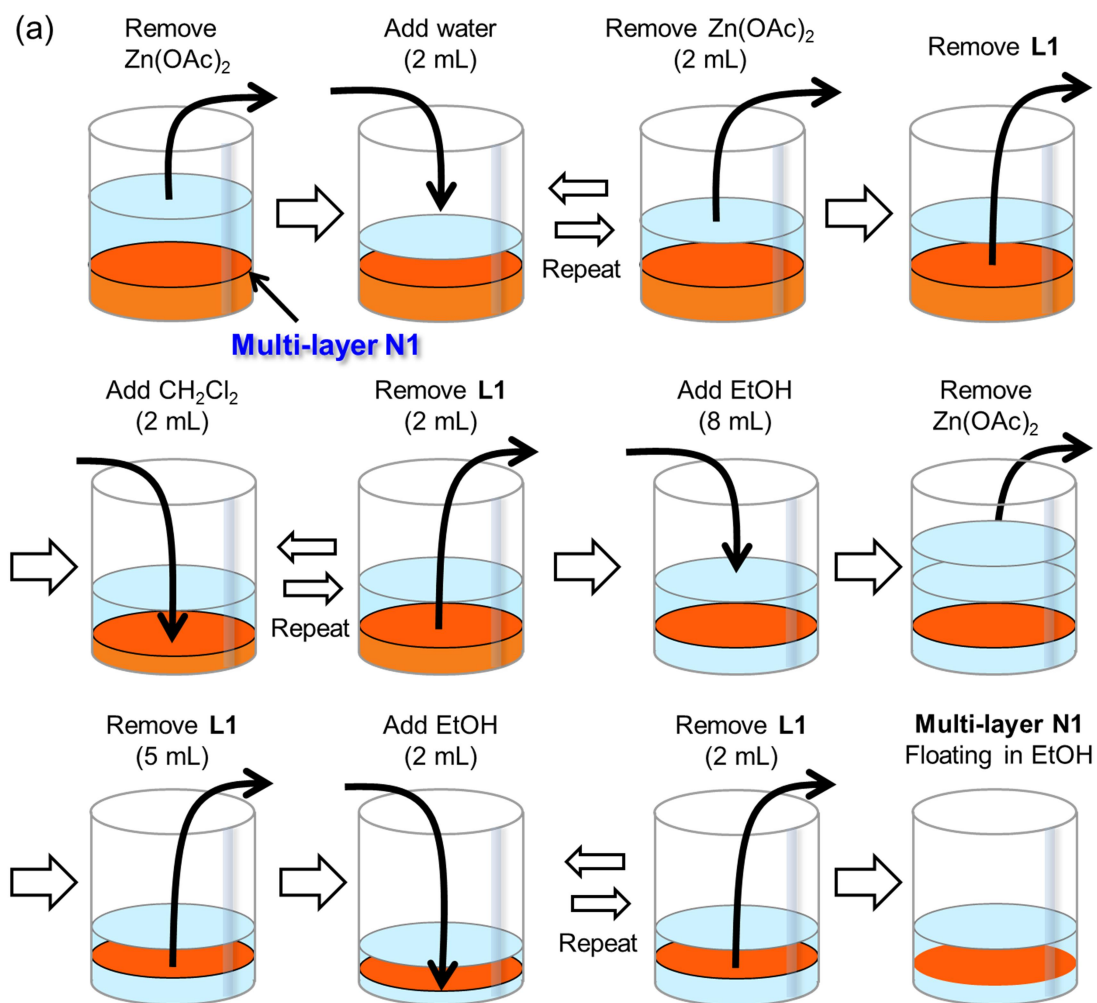
Figure 2-3-2 (a) Schematic illustration of obtaining **multi-layer N1**. (b) Photograph of **multi-layer N1** on an ITO substrate.

2-4 Morphology observation of multi-layer N1

Morphology of **multi-layer N1** was observed by optical microscopy, scanning electron microscopy (SEM), transmission electron microscopy (TEM), and atomic force microscopy (AFM).

2-4-1 Optical microscopy observation

In order to observe **multi-layer N1** by optical microscope it was transferred to an ITO substrate. Optical microscope images are shown in Figure 2-4-1. They reveal several hundreds of micrometer size of flat, homogeneous and sheet-like morphology of **multi-layer N1**. Although there are several wrinkles or cracks in the film, the area with the size of several hundred μm are confirmed in the optical microscopic level resolution. This result suggests the coordination reaction can be successfully limited toward two-dimensional direction and leads to formation of the sheet-like film at the interface.
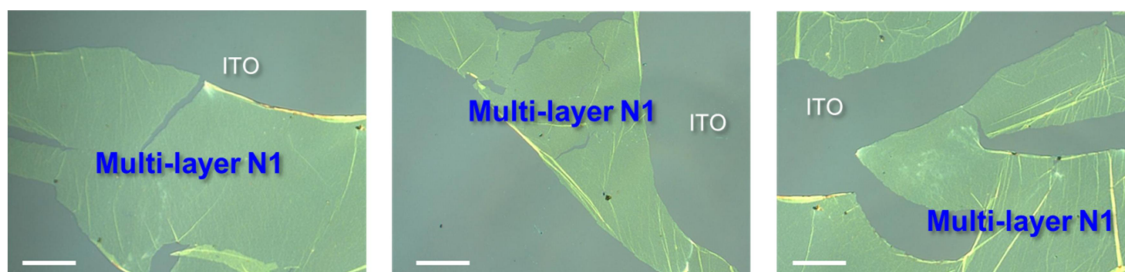
Figure 2-4-1 Optical microscopic images of **multi-layer N1** on an ITO substrate. Scale bar, 50 μm.

2-4-2 SEM observation

Multi-layer N1 for SEM observation was obtained by transferring it to HMDS/Si(111) substrate. The SEM image of Figure 2-4-2 also represents flat and film-like morphology in multi-layer N1 and its size to be almost 100 μm. The observed deflections and cracks also suggest the sheet structure of multi-layer N1. As suggested similarly in optical microscopy observations, this result indicates the limited direction of interfacial reaction produces multi-layer nanosheet.
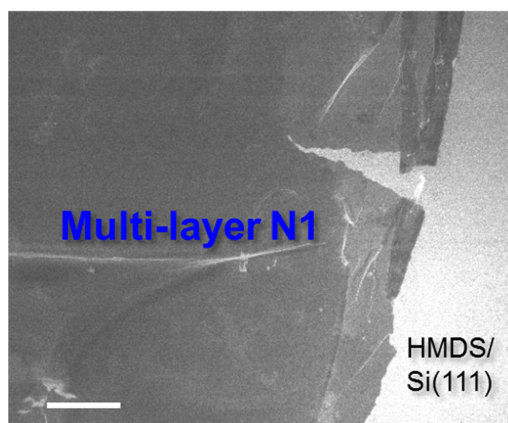
Figure 2-4-2 SEM image of multi-layer N1 on HMDS/Si(111) substrate. Scale bar, 20 μm.

2-4-3 TEM observation

For nanometer scale morphology observation, TEM measurements were performed. Figure 2-4-3 shows the TEM images of **multi-layer N1**. The same as optical microscopy and SEM observations, its sheet-like morphology is also revealed even in several tens of nm scale. Not only flat surface but also several steps near the edge appear in this scale. This suggests the layered structure of **multi-layer N1**. TEM observation result also ensures the construction of two-dimensional homogeneous nanosheets at the interface in several tens of nm scale.
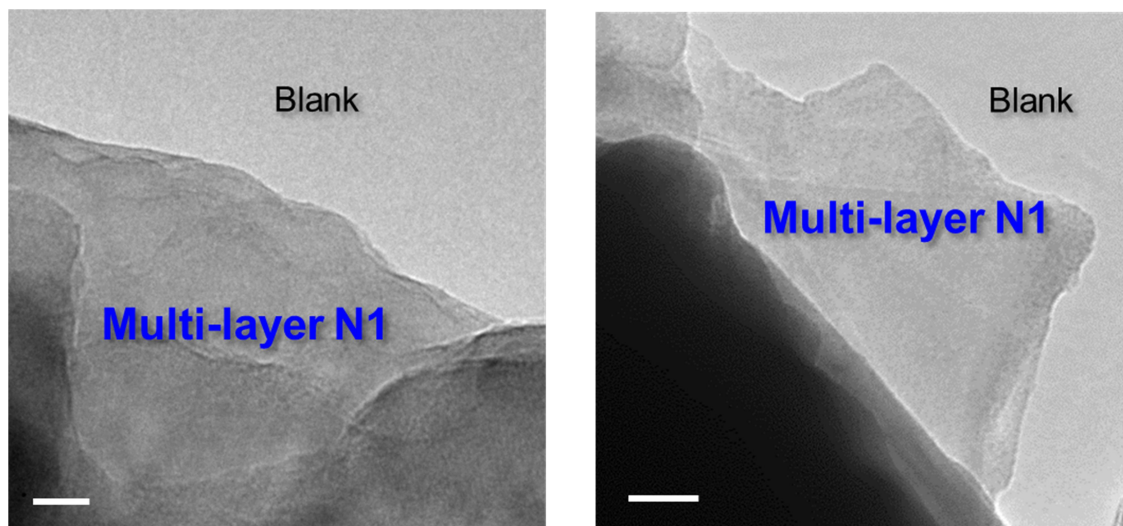
Figure 2-4-3 TEM image of **multi-layer N1**. Scale bar, 10 nm (left) and 50 nm (right).

2-4-4 AFM observation

In order to identify the typical thickness of **multi-layer N1**, I employed AFM observation on HMDS/Si(111) substrate. In this case, concentration of zinc acetate in upper aqueous layer was 0.05 M (20 mL) and **L1** in lower dichloromethane layer was 1.0×10^{-4} M (10 mL), and they reacted for 4 days. The AFM image and its cross-section analysis reveal its flat and uniform morphology, as confirmed similarly in the other microscopy studies. Typical thickness of **multi-layer N1** is 700 nm (Fig 2-4-4). As I mention single-layer thickness in Section 2-9-2, this corresponds to 580 layers of the nanosheet.
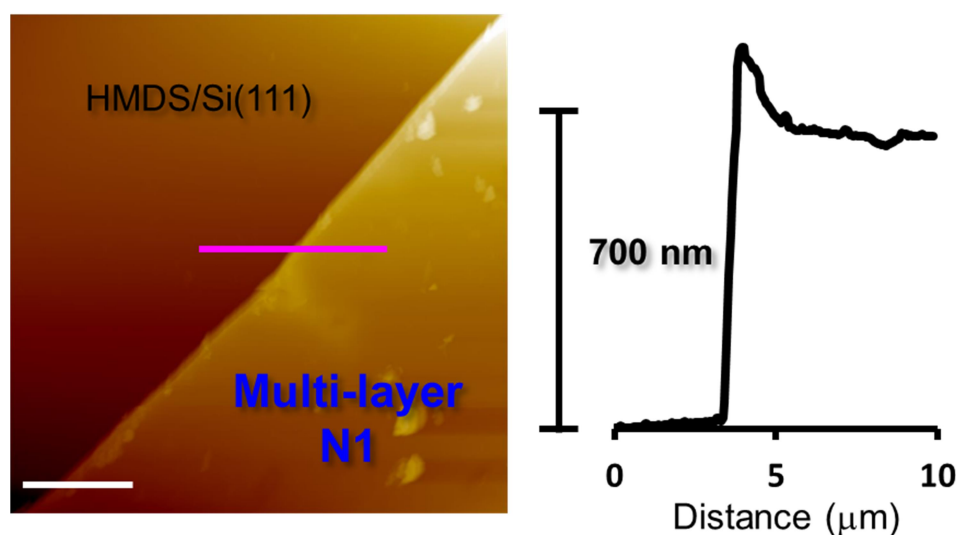
Figure 2-4-4 AFM image of **multi-layer N1** on HMDS/Si(111) substrate and *its* cross-section analysis along the magenta line. Scale bar, 5 μm.

While this is a typical **multi-layer N1** thickness, its controllability was demonstrated by changing the reaction condition such as concentration of **L1**. Figure 2-4-5 shows the thickness control by **L1** concentration. Zinc acetate concentration (0.05 mol/L, 20mL) and reaction time (4 days) in the liquid/liquid interfacial synthesis were the same in all the experiments. It ensures the **multi-layer N1**'s thickness can be controlled from 6 to 800 nm by this method, which is corresponding to 5-670 layers. Both upper and lower limitations can be derived from the encounter limitation of ligand molecules and zinc ions. Produced film disturbs the reaction in the case of upper limitation, and lack of **L1** molecules prohibits the reaction in the case of lower limitation.
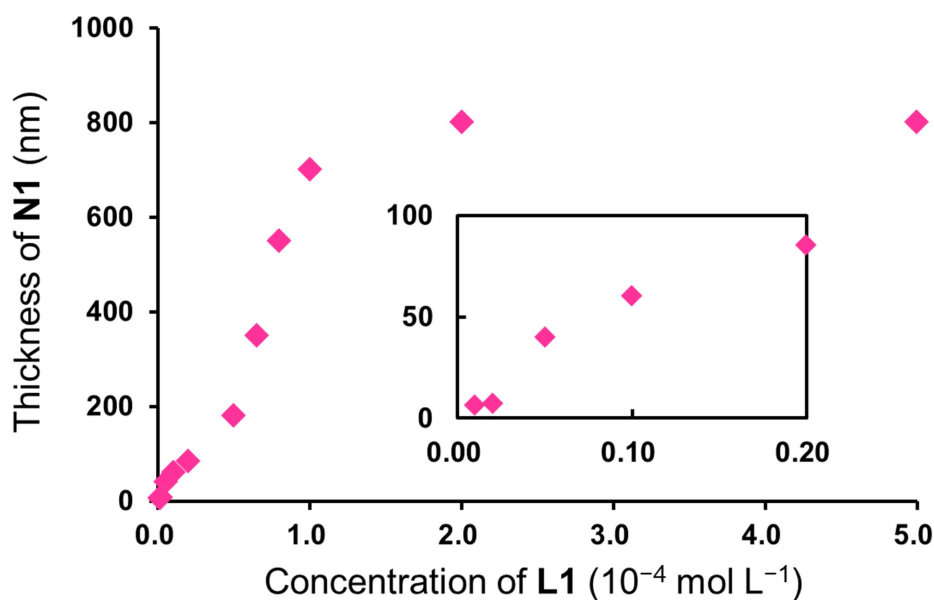
Figure 2-4-5 Control of the thickness based on the concentration of **L1** in the liquid/liquid interfacial synthesis. The inset shows a close-up of the low concentration of **L1**. Reaction time, 4 days. Temperature, room temperature. Concentration of zinc acetate in the upper layer, 0.05 mol/L.

2-5 Constituent elements of multi-layer N1

Multi-layer N1 was transferred to highly ordered pyrolytic graphite (HOPG) for XPS analysis. In order to compare the chemical composition, L1 and a mononuclear bis(dipyrrinato)zinc(II) complex M1 were also measured as references for XPS. The compounds were dissolved in dichloromethane and one droplet of the solution was dropped on HOPG to evaporate the solvent for deposition on the substrate. Figure 2-5-1 shows XPS of these three samples in N $1s$ and Zn $2p_{3/2}$. L1 does not show any Zn $2p_{3/2}$ peaks, while one peak is present in the case of multi-layer N1 and the reference M1. Both multi-layer N1 and the reference M1 represent the similar peak position (1021.6 eV and 1021.8 eV). This suggests the coordination reaction produces the same zinc ion moiety in M1 and multi-layer N1. Also, the spectrum of L1 features two N $1s$ peaks at 400.0 eV and 398.4 eV, which are assignable to pyrrolic and iminic nitrogen atoms respectively[12] (Figure 2-5-2). On the other hand, M1 shows a single N $1s$ peak (398.8 eV) originating from its coordination to the zinc center, which makes the two nitrogen atoms equivalent to one another. Multi-layer N1 displays a single N $1s$ peak and its binding energy exhibits almost the same as M1 (399.0 eV), indicating the same chemical composition as multi-layer N1 and M1. These results ensure the formation of bis(dipyrrinato)zinc(II) complex motif in multi-layer N1.

Furthermore, the abundanc ratio calculated from the peak area corrected using the photoionization cross-section is consistent with the ideal value of N:Zn = 4:1 (N:Zn = 80.6:19.4 for M1 and N:Zn = 80.7:19.3 for multi-layer N1). These findings also support the quantitative construction of bis(dipyrrinato)zinc(II) moiety in multi-layer N1.
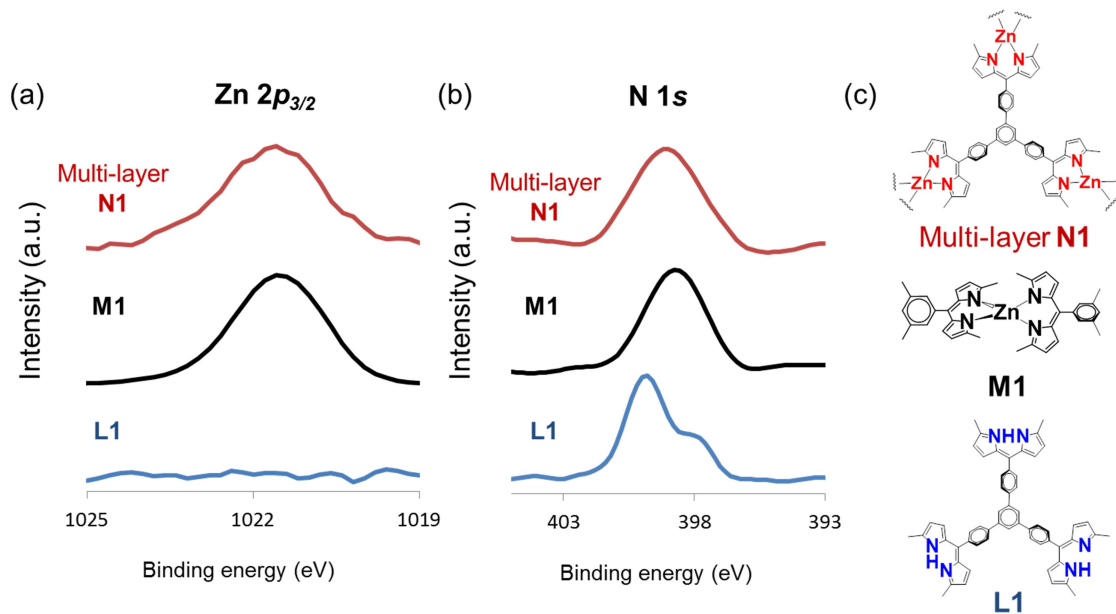
Figure 2-5-1 XPS for **multi-layer N1**, reference **M1**, and **L1**. (a) Narrow-scan XPS focusing on the N 1*s* region. (b) Narrow-scan XPS focusing on the Zn 2*p*$_{3/2}$ region. (c) Chemical structure of **multi-layer N1**, reference **M1**, ligand **L1**.
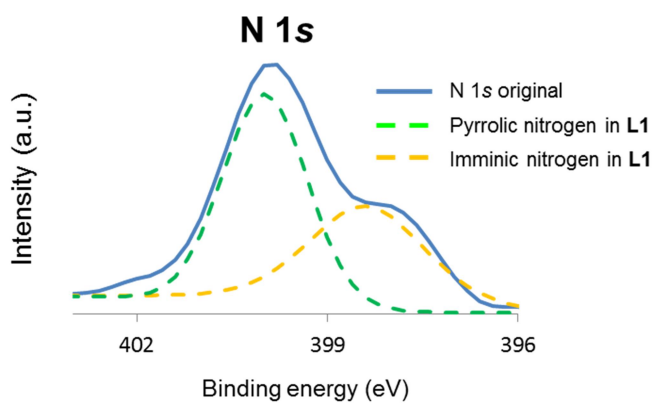

Figure 2-5-2 Peak deconvolution of N 1*s* spectrum for **L1**.

I also conducted the XPS measurements for excluding the possibility of H_2O molecules coordinating to zinc moiety to form a square-pyramidal or octahedral coordination structure. The O $1s$ spectrum is shown in Figure 2-5-3. This time in order to avoid water contamination at the surface of the nanosheet, the sample was subjected to argon sputtering. The lack of O $1s$ peak supports that the coordination structure does not contain any H_2O.
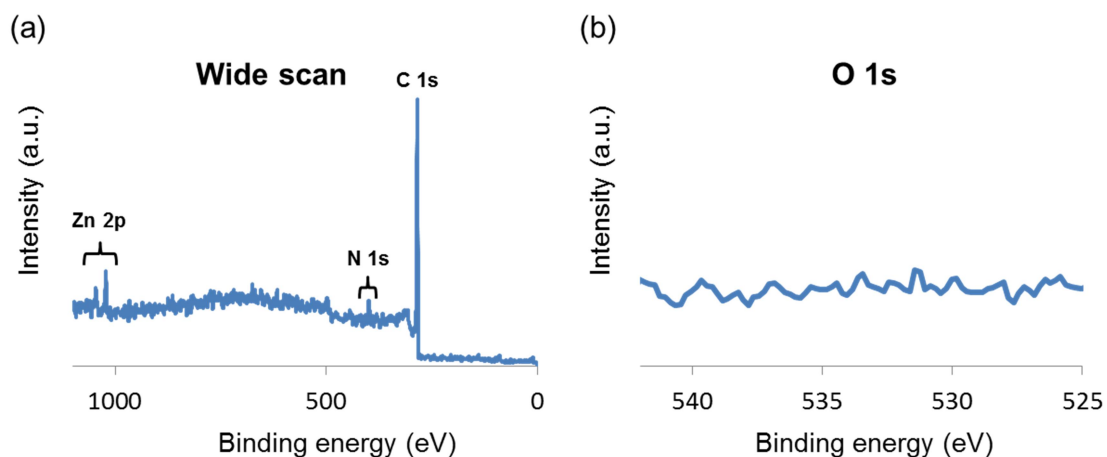
Figure 2-5-3 XPS of **multi-layer N1** on HOPG. (a) Wide-scan. (b) Narrow-scan focusing on the O1s region. The sample was subjected to argon sputtering to remove the contaminated surface by oxygen and water.

2-6 Structure

Multi-layer N1's in-plane periodicity was estimated by selected area electron diffractions (SAEDs) in TEM. Multi-layer N1 synthesized by liquid/liquid interfacial synthesis was deposited to copper grids directly and its edge was focused at room temperature to obtain SAED patterns. A hexagonal in-plane diffraction pattern was observed as shown in Figure 2-6-1. This is consistent with the simulated in-plane diffraction patterns that are optimized using a molecular mechanics calculation. Although lower index diffractions could not be observed because of a direct electron beam, the outside hexagonal pattern was just equal to the simulated three AA-, ABAB-, and ABC- stacking which possess the hexagonal unit cell structure of 3.6 nm for each side (Figure 2-6-2). Hexagonal outside spots are assignable to (15,0,0) (0,15,0) (15,-15,0) (0,-15,0) (-15,0,0) (-15,15,0). This result represents the hexagonal in-plane periodicity of multi-layer N1 and its lattice constants of 3.6 nm.
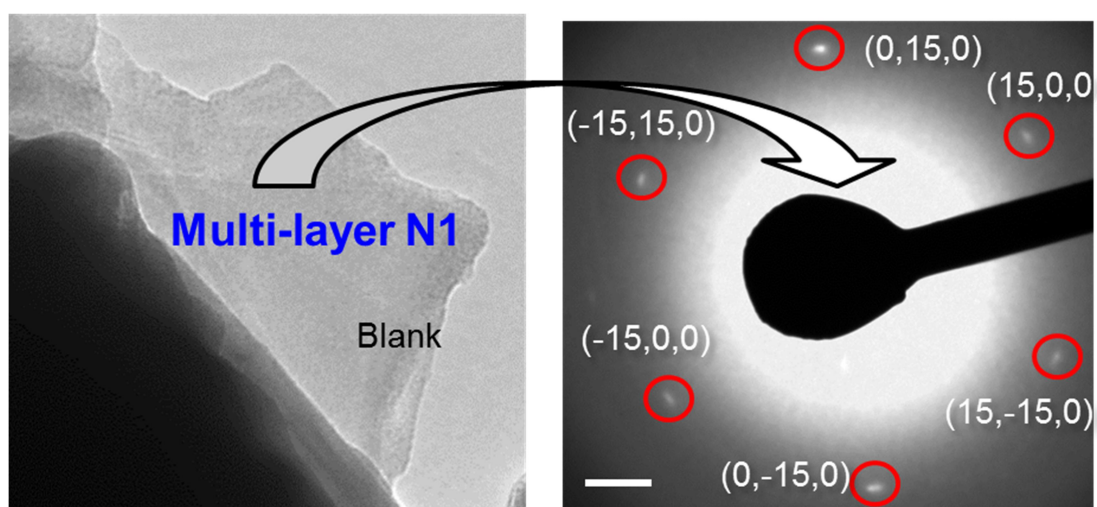
Figure 2-6-1 TEM/SAED pattern of **multi-layer N1**. Recorded with a nominal camera length of 20 cm. Scale bar, 2 nm^{-1}.
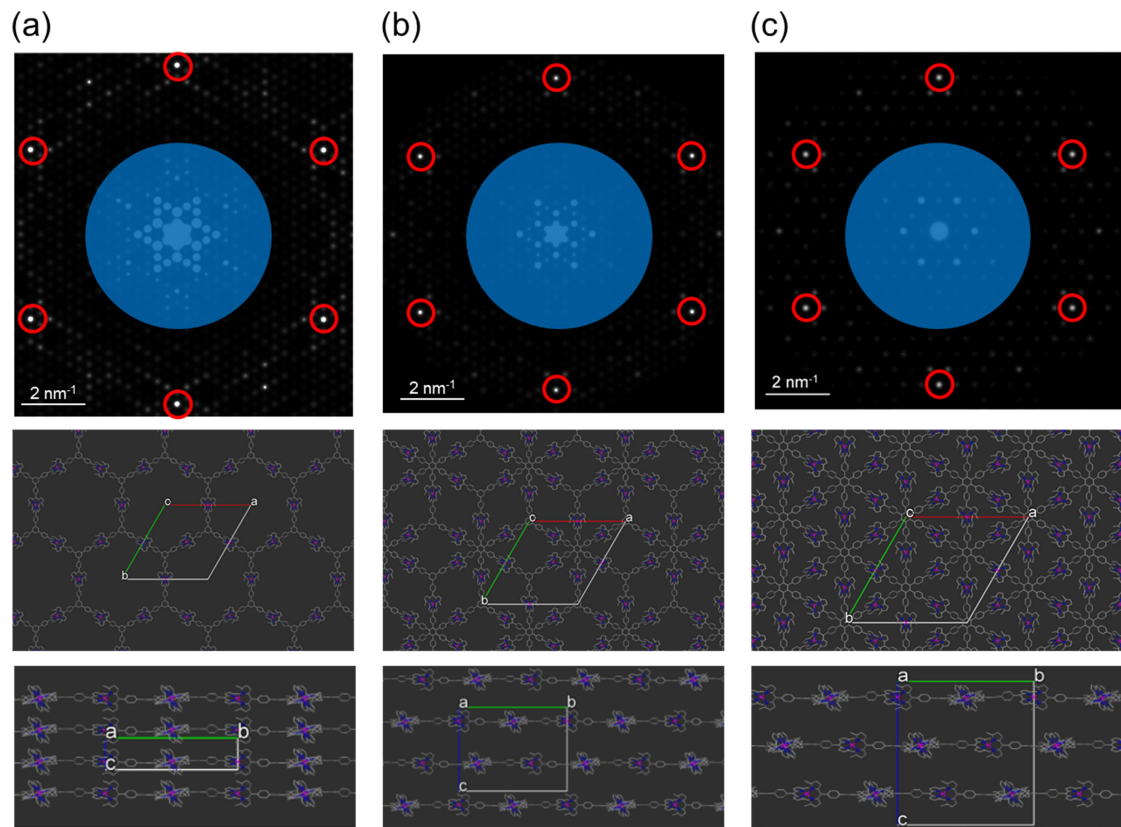
Figure 2-6-2 Optimized three-dimensional lattices and its SAED simulation of **multi-layer N1**. (a) AA-stack structure (a=35.9 Å, b=35.8 Å, c=7.46 Å, α=ß=90°, γ=120°). (b) AB-stack structure (a=36.0 Å, b=35.9 Å, c=24 Å, α=ß=90°, γ=120°). (c) ABC-stack structure (a=35.8 Å, b=35.8 Å, c=34.5 Å, α=ß=90°, γ=120°). A direct beam disturbs observation of the lower index diffractions (blue circle).
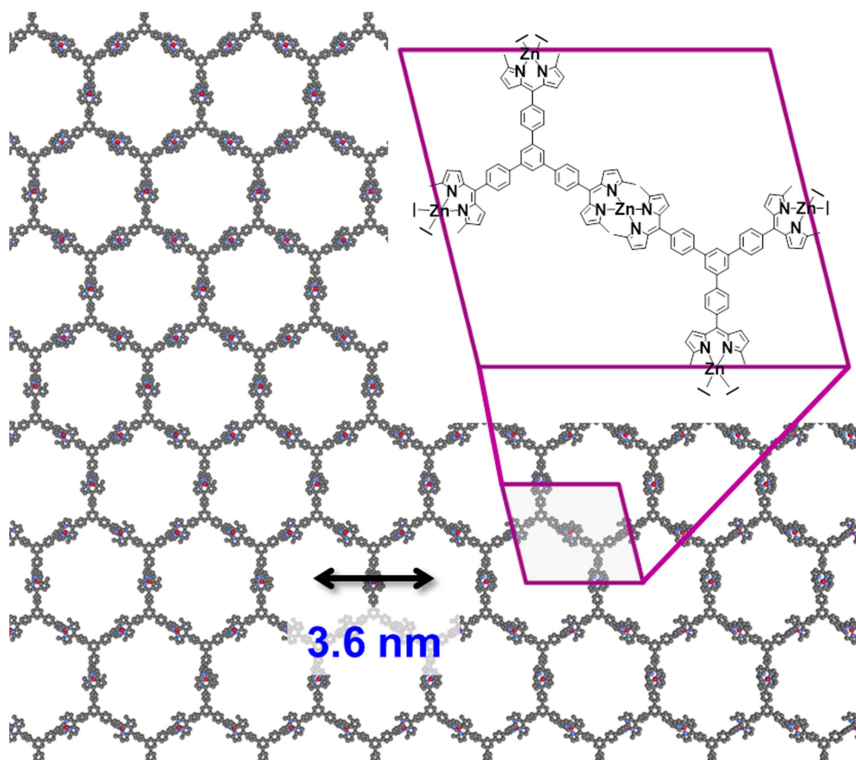
Figure 2-6-3 Illustration of bis(dipyrrinato)zinc(II) nanosheet derived from SAED result. The hexagonal in-plane periodicity was confirmed as ca. 3.6 nm.

2-7 Guest inclusion

　The coordination polymers with empty pore can include guest molecules into the space to demonstrate molecular storage or sensor[13]. **Multi-layer N1** also incorporates the large hexagonal pores in its structure so that guest molecules could be included to the nanosheet. This time Rhodamine-B inclusion was performed because of its appropriate size (16 Å for diameter[14]) and easy detection by its fluorescence. **Multi-layer N1** was deposited on transparent substrates (quartz and ITO) and immersed in a dichloromethane solution of Rhodamine-B (5.0×10^{-5} mol/L) for 15 h. After washing the samples by dichloromethane until the solvent color disappeared, it gave **multi-layer N1** containing Rhodamine-B. The color changed from orange to red, suggesting the successful inclusion of Rhodamine-B in **multi-layer N1** (Figure 2-7-1 (a)). Figure 2-7-1 (b) shows a photograph of **multi-layer N1** with Rhodamine-B under black light with a wavelength of 365 nm. The observed yellow fluorescence was derived from Rhodamine-B, so these results suggest the successful inclusion of Rhodamine-B. **Multi-layer N1** containing Rhodamine-B exhibited the fluorescent peak wavelength at 581 nm corresponding to the fluorescence of Rhodamin-B itself[15].
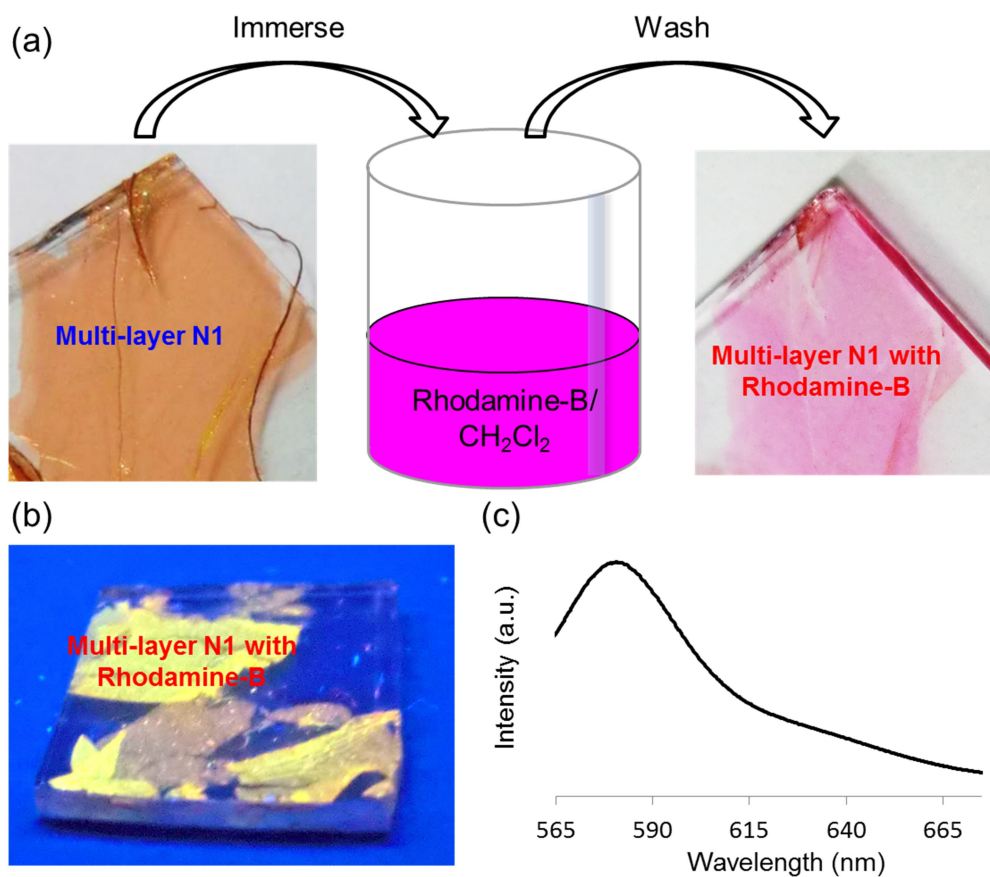
Figure 2-7-1 (a) Schematic illustration of Rhodamine-B immersion in **multi-layer N1** on an ITO substrate. The sample was washed by dichloromethane until its color disappeared. (b) Photographs of **multi-layer N1** with Rhodamine-B on a quartz substrate under black light with a wavelength of 365 nm. (c) Fluorescence spectrum of **multi-layer N1** with Rhodamine-B on a quartz substrate upon excitation with 543-nm light.

2-8 Fabrication of single-layer N1

Previous results reveal the two-dimensional bis(dipyrrinato)zinc(II) nanosheets fabrication. For the synthesis of nanometer thickness of the nanosheets, I performed small scale liquid/liquid interfacial synthesis. In this method, small amount (5 μl) of **L1** was reacted to zinc ions at the interface of mixed organic solvent droplet and aqueous solution. Its reaction could be limited to two-dimensional direction toward the interface to produce two-dimensional nanometer thickness nanosheets at air/liquid interface.

This time **L1** was dissolved in mixture solvent of dichloromethane and ethyl acetate (14:1). By adding a little ratio of ethyl acetate, one droplet of the solution can spread uniformly at the interface. **L1** solution was then sprinkled drop by drop (almost 1 μL for one droplet) to the interface of aqueous solution of zinc acetate in 50-mL glass vial (4.0 cm in diameter). For obtaining **single-layer N1**, 5.0 μL of **L1** solution was used (7.4×10^{-5} mol/L). The amount of **L1** solution and concentration were determined as follows.

In one unit cell of **N1** contains two **L1** molecules so that **L1**'s density is calculated as follows.

$$\frac{\dfrac{2}{6.02 \times 10^{23}}}{(3.6 \times 10^{-9})^2 \times \dfrac{\sqrt{3}}{4} \times 2} = 3.0 \times 10^{-7} \text{ mol/m}^2$$

In order to cover whole surface of the glass vial (4.0 cm in diameter) by monolayer nanosheet, the amount of **L1** is calculated as below.

$$3.0 \times 10^{-7} \times \pi \times (2.0 \times 10^{-2})^2 = 3.7 \times 10^{-10} \text{ mol}$$

When I sprinkle **L1** solution for 5 μL, **L1** concentration is determined to be

$$\frac{3.7 \times 10^{-10}}{5 \times 10^{-6}} = 7.4 \times 10^{-5} \text{ mol/L}$$

The reaction system was kept calm for more than 4 hours to evaporate the mixed solvent and the nanosheets construction. Then **single-layer N1** at the interface was transferred to several substrate (HMDS/Si(111), quartz, SnO$_2$) by Langmuir–Schäfer method. **Single-layer N1** on each substrate was then washed by pure water, ethanol, and dichloromethane to remove zinc acetate and **L1**. Nanosheet, **N1** was insoluble in these solvents because of its polymeric structure.
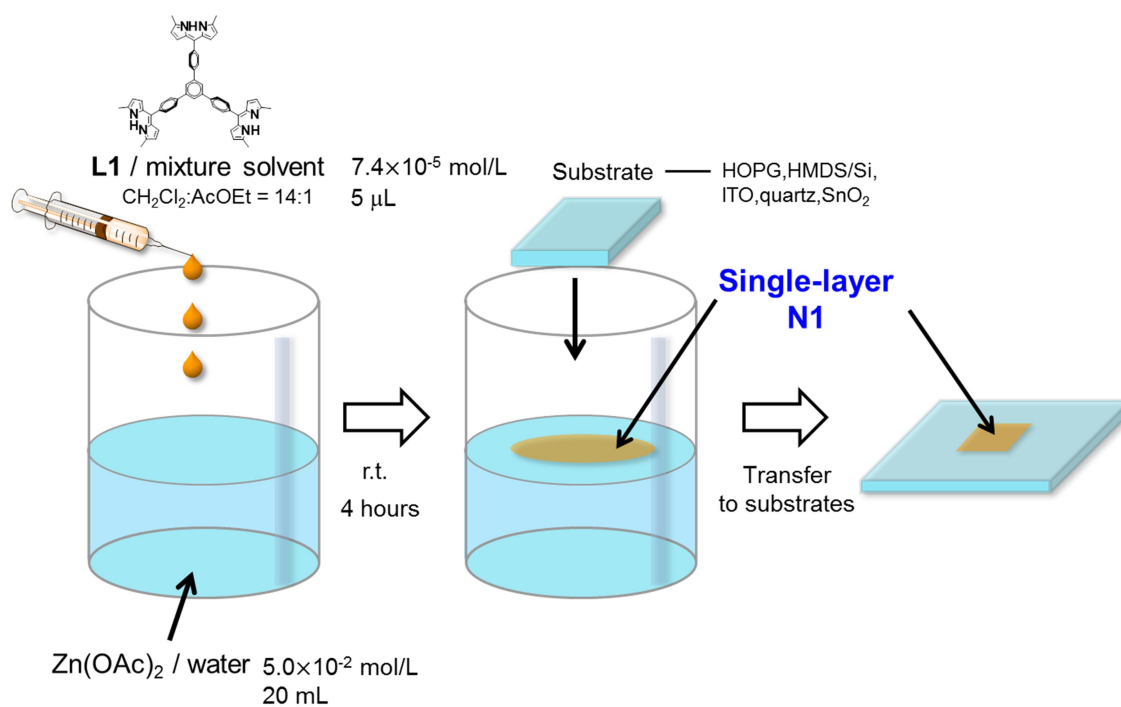

Figure 2-8-1 Schematic illustration of small scale interfacial synthesis of **single-layer N1** and its transfer process.

2-9 Morphology observation of single-layer N1

Obtained **single-layer N1** was then observed by AFM in order to reveal its morphology and size. Its atomically thickness was also confirmed by AFM scratching method.

2-9-1 Morphology and size of the nanosheet

The AFM analysis disclosed the flat sheet texture and morphology of **N1**. Figure 2-9-1 shows the height and phase images of **N1** on an HMDS/Si(111) substrate. The phase image clearly distinguishes **N1** and the bare substrate: the nanosheet possesses a phase value lower by 2.4°. The height image reveals a homogeneous area with more than 10 μm in each side in **N1**. In fact this size is significantly larger than that in other CONASHs such as bis(dithiolato)nickel nanosheets (~1 μm). In the case of bis(dithiolato)nickel nanosheets, the complexation reaction of dithiolene ligand and nickel(II) ions is not reversible and its complex unit is not neutral so that it needs counter cation (Na$^+$) for nanosheet fabrication[16]. In another case, bis(terpyridine)metal nanosheets do not produce single-layer nanosheets, which are cationic character and require counter anions (BF$_4^-$) for nanosheets fabrication[17]. On the other hand, the coordination reaction of dipyrrin ligands with metal ions is spontaneous and reversible in forming the bis(dipyrrinato)zinc(II) complex[9]. For this feature, the nanosheets can grow with recovering their defects, thereby constructing large homogenous area. Furthermore, different from two other examples above, the bis(dipyrrinato)zinc(II) complex unit has neutral character and it does not require any counter ions for nanosheet synthesis. This feature can contribute to fabricate a large size nanosheet because we don't need to suffer from the counter ions that can disturb the nanosheet growth at the interface. Also its mild reaction condition (under air, room temperature) is advantage to fabricate huge size of the nanosheet.

An enlarged AFM view (Figure 2-9-1 (b)) reveals **N1** not to be aggregation of a lot of particles.
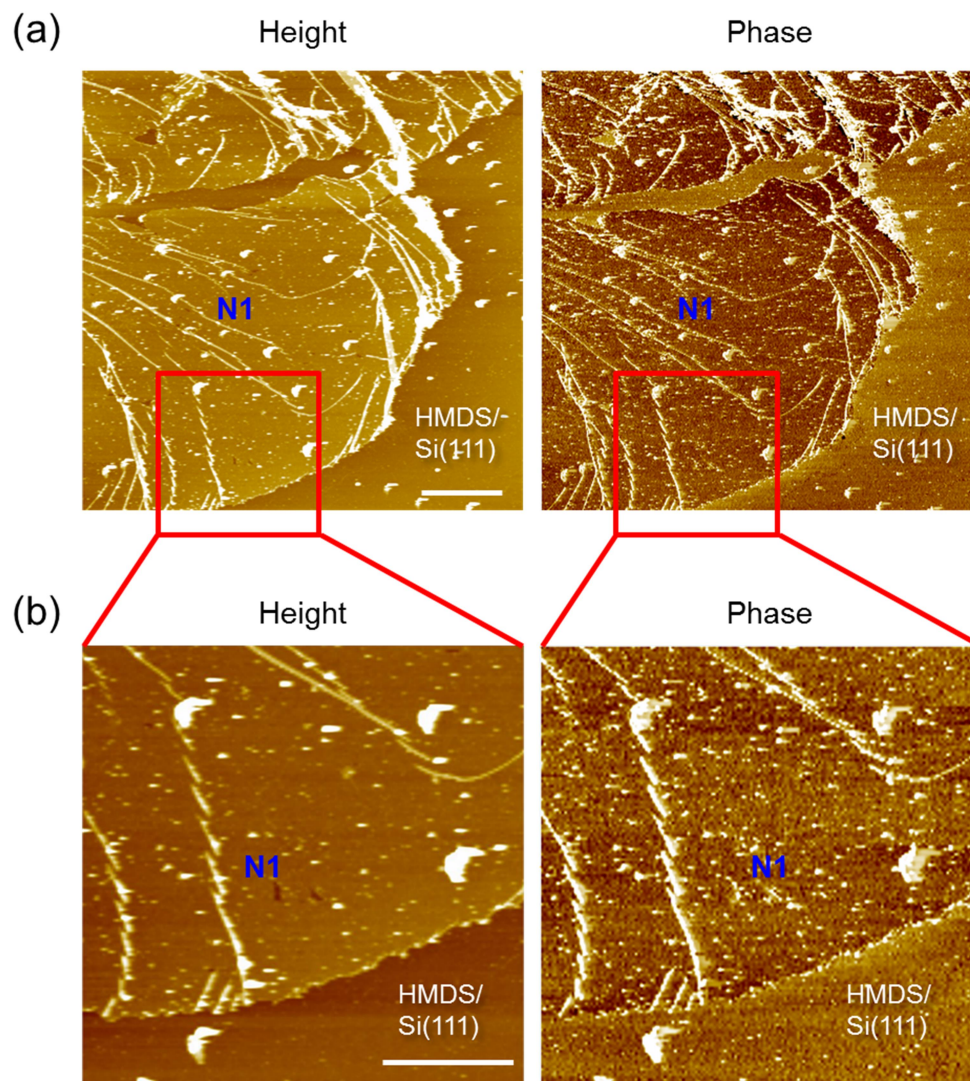
Figure 2-9-1 (a) Height and phase images of **N1**. Scale bar, 3 μm. (b) Enlarged AFM images of **N1**. Scale bar, 2 μm.

2-9-2 Thickness of **single-layer N1**

  In order to confirm the single-layer nature of the nanosheet, part of **N1** was scratched with the AFM tip at a force of 8.6×10^2 nN. Figure 2-9-2 shows the height images before and after scratching, and the scratched region is highlighted with a green square. This treatment resulted in the removal of **N1**, leaving an intact HMDS/Si(111) surface. A cross-section analysis of one of the scratched edges reveals **N1** thickness to be 1.2 nm. Lack of steps at scratched edge side ensures the nanosheet to be a single-layer (**single-layer N1**). A higher-force scratch (1.2×10^4 nN) resulted in a more drastic change in the AFM image and both **single-layer N1** and the HMDS/Si (111) surface were scratched.
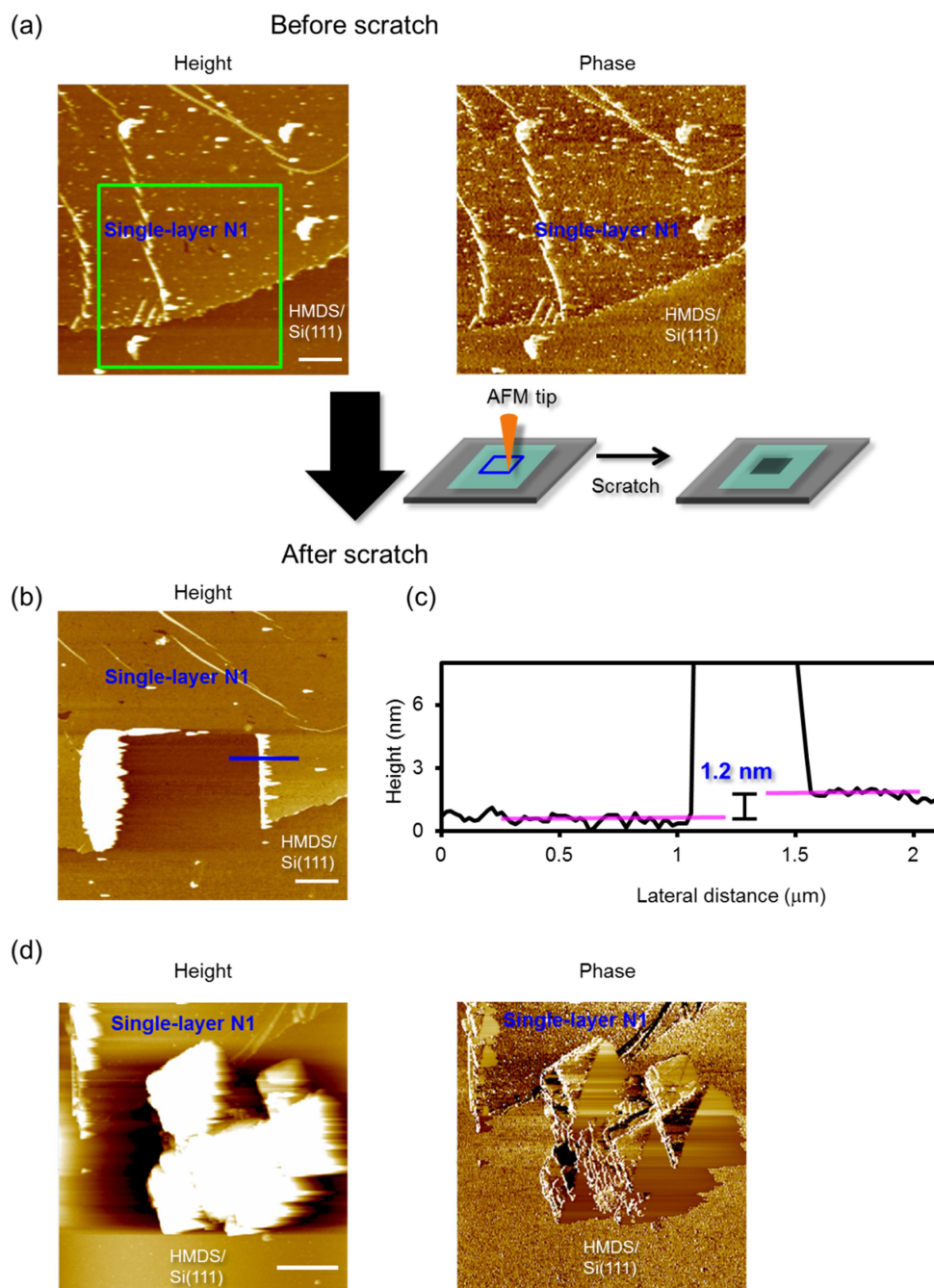
Figure 2-9-2 (a) Height and phase images of **single-layer N1** before a scratch by the AFM tip. Scale bar, 2 μm. (b) Height images of **single-layer N1** after a scratch. Scale bar, 1 μm. (c) Cross-section analysis at one of the steps in the scratched region (shown as a blue line in (b)) (d) Height and phase images after a scratch by an AFM tip at a larger force. Scale bar, 1 μm.

2-10 Constituent elements of single-layer N1

In order to assess constituent elements and bonding properties of **single-layer N1**, XPS was conducted. **Single-layer N1** was transferred to HMDS/Si(111) for XPS measurements. Figure 2-10-1 shows XPS results of **single-layer N1**, a ligand **L1**, and a reference mononuclear complex **M1** on HOPG substrate. In the case of Zn $2p_{3/2}$ spectra, **L1** does not show any peaks, whereas there is a single peak in **single-layer N1** and a reference **M1**. Both of them reveal the same binding energy (1021.8 eV), suggesting that the coordination reaction produces the same zinc ion motif in **M1** and **single-layer N1**. Moreover, the spectrum of **L1** features two N $1s$ peaks at 400.0 eV (pyrrolic nitrogen) and 398.4 eV (iminic nitrogen), while **M1** and **single-layer N1** feature only a single N $1s$ peak nearly at the same position (399.0 eV and 398.8 eV). This difference originates from coordination reaction between zinc(II) ion and **L1**, which makes the two nitrogen atoms equivalent to one another. These findings reveal the formation of bis(dipyrrinato)zinc(II) complex motif in **single-layer N1**.

Single-layer N1 and **multi-layer N1** were almost identical in the peak numbers and positions of Zn $2p_{3/2}$ (single peak at 1201.8 eV and 1201.6 eV) and N $1s$ (single peak at 398.8 eV for both). This result indicates that **single-layer N1** is composed of bis(dipyrrinato)zinc(II) complex units, as was confirmed in **multi-layer N1.**

Furthermore, the quantitative analysis was performed from the peak area of each element's spectrum. The calculated abundance ratio of nitrogen and zinc atoms is consistent with the ideal value of N:Zn = 4:1 and **single-layer N1** (N:Zn = 80.6:19.4). It also supports the quantitative construction of bis(dipyrrinato)zinc(II) complex in **single-layer N1**.
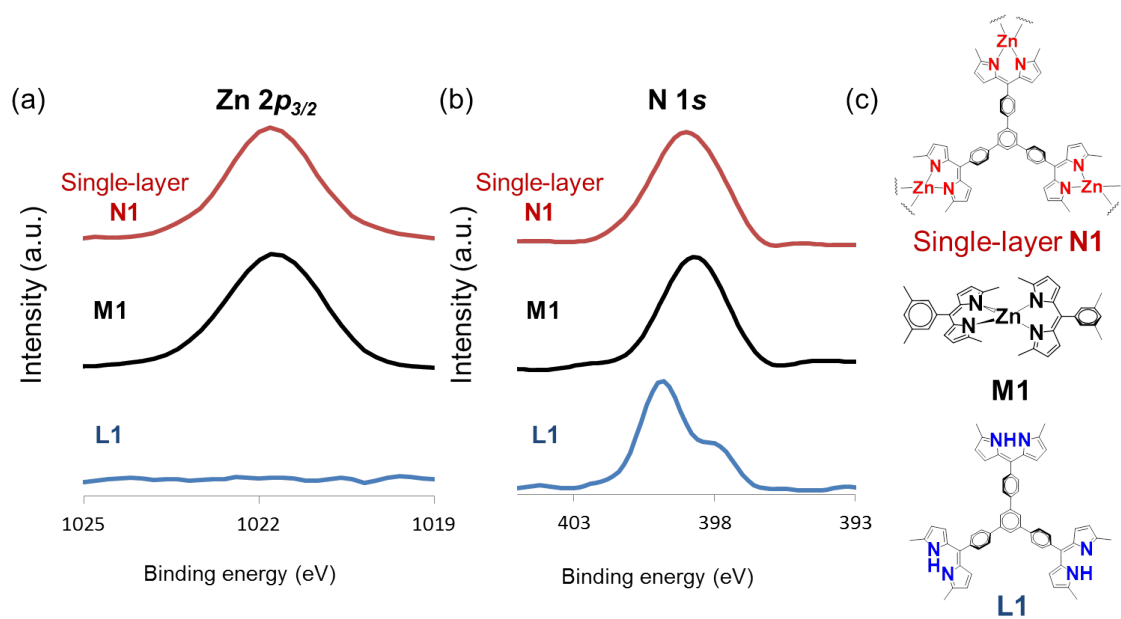
Figure 2-10-1 XPS for **single-layer N1**, reference **M1**, and **L1**. (a) Narrow-scan XPS focusing on the N 1*s* region. (b) Narrow-scan XPS focusing on the Zn 2*p*₃/₂ region. (c) Chemical structure of **single-layer N1**, reference **M1**, ligand **L1**.

2-11 In-plane periodicity of single-layer N1

In order to disclose in-plane periodicity of **single-layer N1**, scanning tunneling microscopy (STM) was employed. For this measurement **single-layer N1** was synthesized by small scale liquid/liquid interfacial synthesis and transferred to HOPG substrate. Figure 2-11-1 shows a hexagonal in-plane periodicity and its size of 7.98 nm. Actually this size is too large to assign as the direct structure of **single-layer N1** (3.6 nm, Figure 2-6-3), which indicates that the observed hexagonal pattern is derived from moiré interface between two hexagonal lattices, HOPG (0.246 nm) and **single-layer N1**. The hexagonal moiré pattern represents **single-layer N1**'s in-plane hexagonal structure.

A moiré structure with hexagonal periodicity of 7.98 nm is created by the two hexagonal lattices, one is **single-layer N1** and the other is HOPG. The moiré lattice vector $\mathbf{M_1}$ can be represented as

$$\mathbf{M_1} = m\mathbf{a_1} + n\mathbf{a_2} = m_0\mathbf{b_1} + n_0\mathbf{b_2} \qquad (1)$$

where m, n, m_0, and n_0 are intergers, and $\mathbf{a_1}$, $\mathbf{a_2}$ are unit lattice vectors for HOPG ($|\mathbf{a_1}| = |\mathbf{a_2}| = 0.246$ nm) and $\mathbf{b_1}$, $\mathbf{b_2}$ are those for **single-layer N1**. In this case only $(m, n, m_0, n_0) = (13, 14, 2, 3)$ can satisfy the SAED results (Section 2-6), and its in-plane periodicity is determined as 3.6 nm. The rotation angle between HOPG and **single-layer N1** is estimated as 2.6° from equation (1).
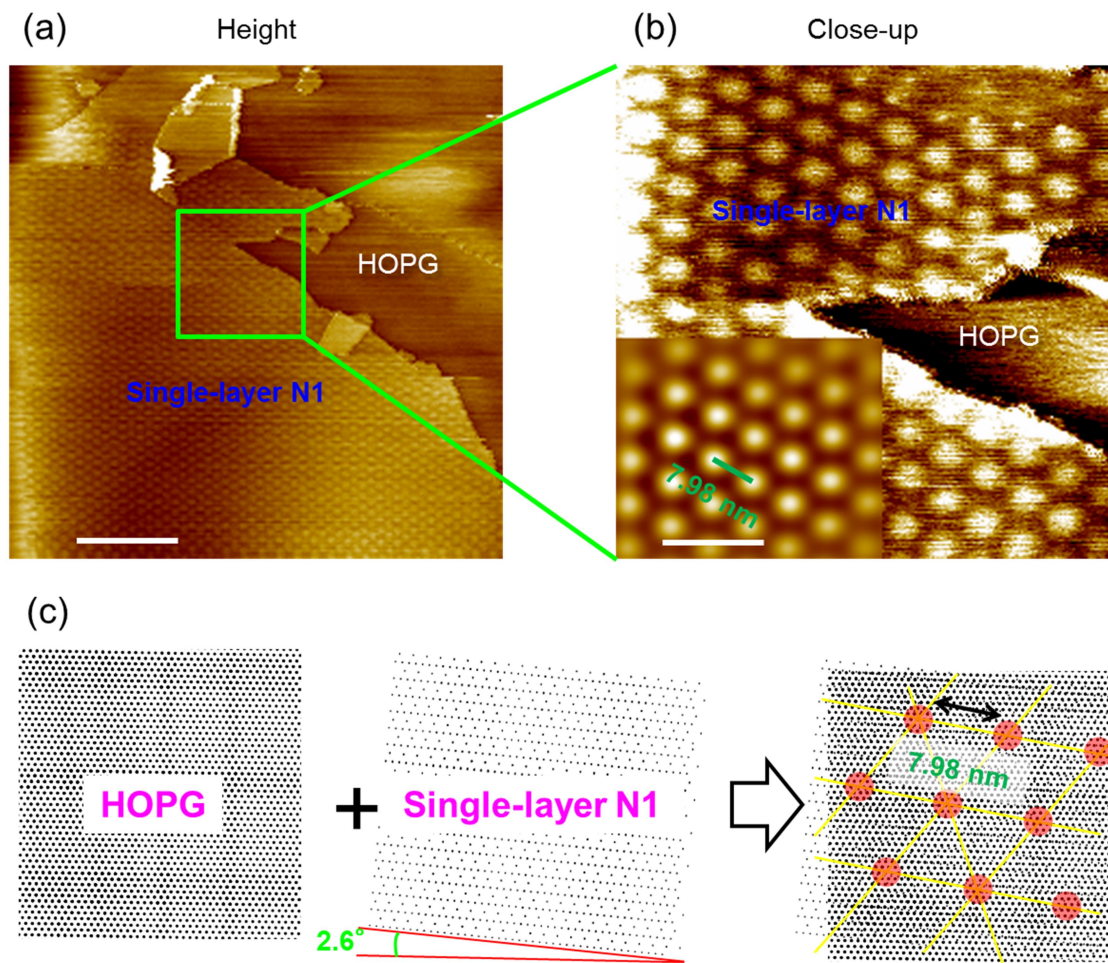
Figure 2-11-1 (a) STM height image of **single-layer N1** exhibiting a hexagonal pattern. Scale bar, 100 nm. (b) Close-up of the height image. The bottom left corner shows a fast Fourier transform (FFT)-filtered image. Scale bar, 20 nm. (c) Schematic illustration of the overlap between **single-layer N1** and the HOPG lattice that produces the observed moiré superlattice. The rotation angle is 2.6°.

2-12 Fabrication and observation of several-layer N1

A small scale liquid/liquid interfacial synthesis can not only used for single-layer nanosheets fabrication but also for **several-layer N1** fabrication. For this synthesis, the amount of a **L1** solution was increased from 5 μL to 20 μL in the interfacial synthesis system (4 layers of the nanosheet was ideally produced). After spontaneous evaporation of the organic solvent, the system was undisturbed to obtain **several-layer N1** at the air/liquid interface. **Several-layer N1** on a flat substrate was then subjected to several analyses.

An AFM image of **several-layer N1** is shown in Figure 2-12-1. The figure reveals large homogenous area, the same as **single-layer N1**. The phase image is flat, whereas the topological image reveals steps and divided area. This result indicates that the scanned area was completely covered with **several-layer N1**.
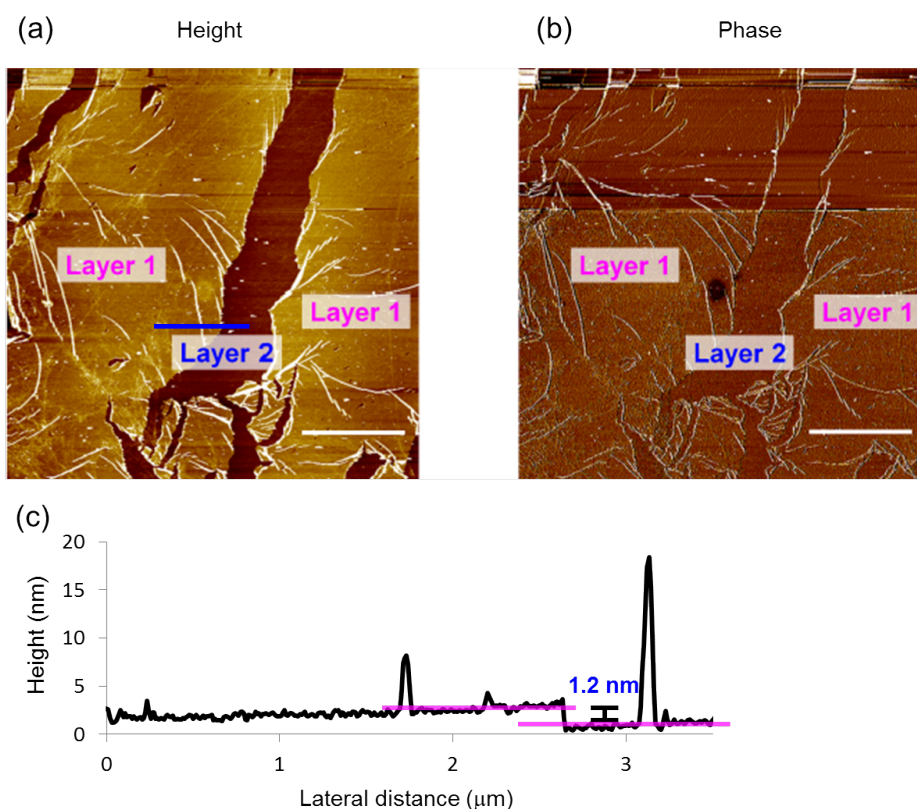
Figure 2-11-1 (a) AFM height image of **several-layer N1** with large homogeneous area on HMDS/SI(111). At least two-layers can be recognized (Layer 1 and 2). (b) Phase image of **several-layer N1**. The flat phase image ensures both layers to be **N1**, covering the entire surface in the scanned region. Scale bar, 5 μm. (c) Cross-section analysis at one of the steps between layer 1 and layer 2 (shown as a blue line in (a))

2-13 Photofunction of N1

Previous results reveal single-layer bis(dipyrrinato)zinc(II) CONASH can be fabricated by small scale liquid/liquid interfacial reaction and its size is larger than other CONASHs. Following the successful nansoheet fabrication, I tried demonstration of the nanosheets' new function, that is photofunction which is intrinsic in bis(dipyrrinato)zinc(II) complex motif. The notable photofunction was introduced to the nanosheets to generate efficient photocurrent.

2-13-1 Preparation of stacked **single-layer N1**

For studying new function of bis(dipyrrinato)zinc(II) nanosheets, I performed layering of **single-layer N1** to construct stacked **single-layer N1**. A Langmuir-Blodgett trough was used as a reaction container and an aqueous solution of zinc acetate (0.05 mol/L, 61mL) was filled the trough. Then a mixture solution (dichloromethane: ethyl acetate = 14:1) of **L1** (7.4×10^{-5} mol/L, 27.7 μL) was sprinkled to the air/liquid interface. In this condition **single-layer N1** covered 90% of trough area ideally. The reaction system was kept calm for 4 hours to evaporate solvent and **L1** reacted with the zinc ions. After that the trough was compressed to reach 69.8 cm^2 (90% of the initial trough area) for covering **single-layer N1** whole trough area at a surface pressure of 0.04 mN/m. **Single-layer N1** at the interface was transferred to several substrates (quartz, SnO$_2$) for 1 minute by Langmuir–Schäfer method and it was washed by pure water, ethanol, and dichloromethane. Then the next transfer was employed at the same way by keeping the surface pressure 0.04 mN/m for preserving surface coverage of **single-layer N1**. Repeating this process produced layering of **single-layer N1** (stacked **single-layer N1**).

7.4×10^{-5} mol/L
27.7 μL

L1 / mixture solvent
CH$_2$Cl$_2$:AcOEt = 14:1

Zn(OAc)$_2$/water

r.t.
4 hours

Single-layer **N1**

→ Compression ←
90 %

0.04 mN/m
Substrate

Stacked single-layer **N1**
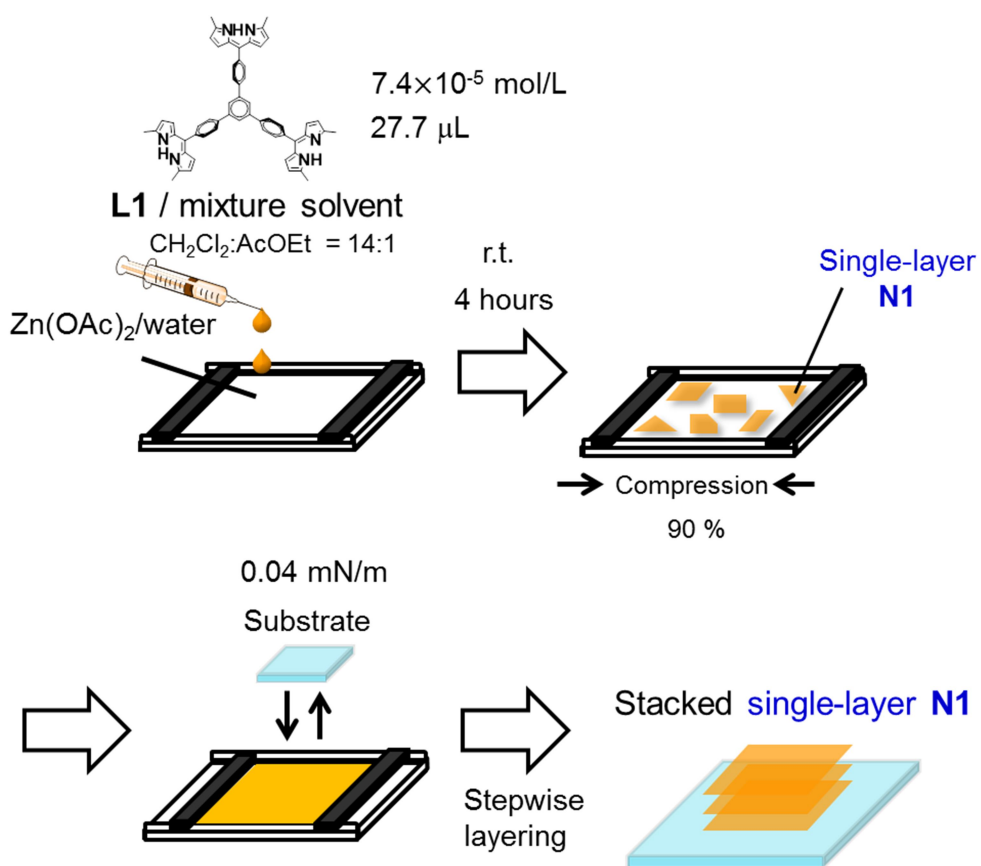
Stepwise layering

Figure 2-13-1 Schematic illustration of stepwise layering **single-layer N1**.

2-13-2 UV/vis absorption spectra

At first optical property of stacked **single-layer N1** was investigated by UV/vis absorbance measurements. Figure 2-13-2(a) shows the UV/vis spectra of **L1**, **M1**[5] and a stacked **single-layer N1**. The ligand **L1** displays an intense absorption band at 446 nm, which is derived from the $^1\pi$–π^* transition of the dipyrrin π-system. Complexation reaction between the dipyrrin ligand and zinc ions is known to induce a redshift of the $^1\pi$–π^* transition band; indeed, the $^1\pi$–π^* transition band in the absorption spectrum of **M1** displays a 49-nm wavelength redshift relative to that of **L1**. Stacked **single-layer N1** also shows an absorption peak attributed to the $^1\pi$–π^* transition in the visible region, and the peak wavelength was much closer to that of **M1** rather than **L1** (54-nm redshift relative to **L1**). This result indicates the coordination reaction between **L1** and the zinc ions in stacked **single-layer N1**.

Then in order to estimate single-layer absorbance, stepwise layering of **single-layer N1** was performed. Figure 2-13-2(b) reveals the ultraviolet/visible spectra of the modified quartz substrate. The peak absorbance at 500 nm ($^1\pi$–π^* transition band of ligand unit) is proportional to the deposition cycles, suggesting the quantitative, layer-by-layer accumulation of **single-layer N1** to fabricate a stacked **single-layer N1**. The slope is calculated as 1.01×10^{-3}, exhibiting single-layer absorbance of the nanosheet. In fact the single-layer absorbance can be estimated as 7.10×10^{-4} from molar extinction coefficient of bis(dipyrrinato)zinc(II) motif[15] and its unit cell size (Figure 2-6-3(c)), so that it ensures that the calculated value is appropriate for the single-layer absorbance.
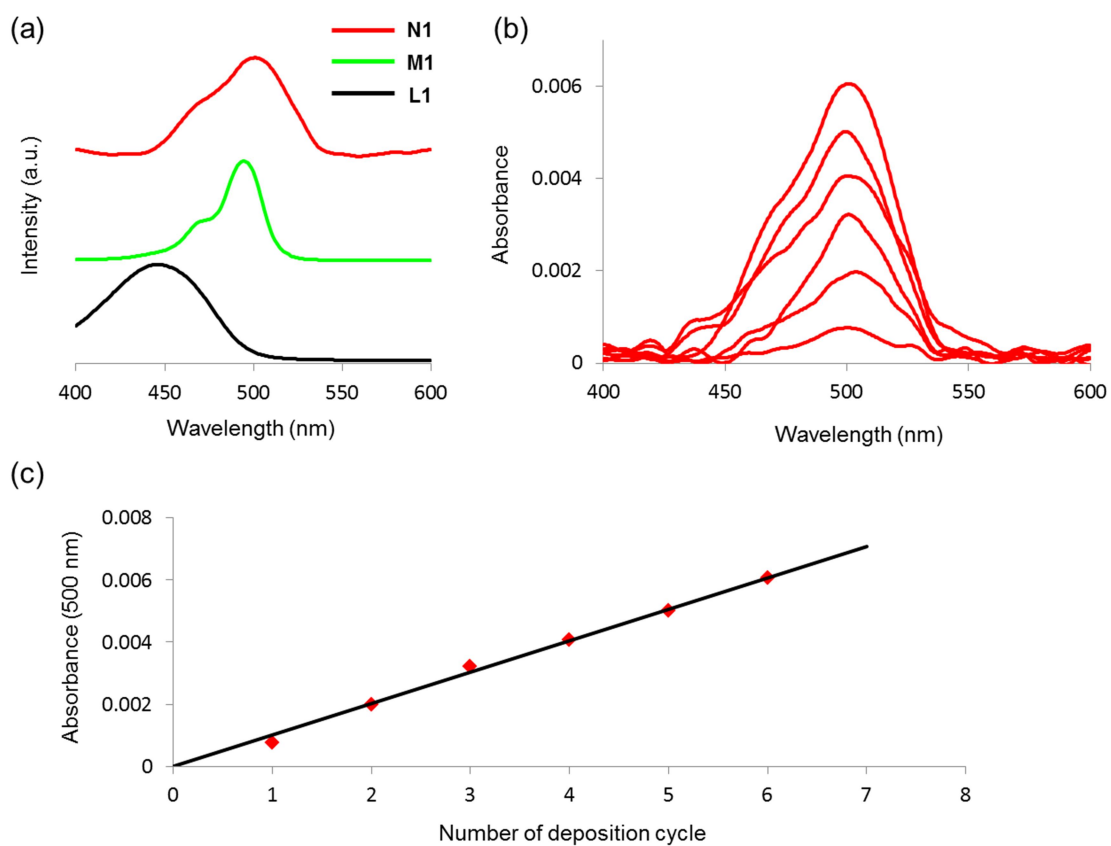
Figure 2-13-2 UV/vis spectroscopy. (a) Spectra of **L1**, **M1** in toluene and stacked **single-layer N1** on a quartz substrate. (b) Spectral change on stepwise depositions of **single-layer N1** on a quartz substrate. (c) Linear relationship between the absorbance at 500 nm and the number of deposition processes. The black line corresponds to the least squares linear fit of the plots.

2-13-3 Photoelectric conversion system

  Electrochemical property of a stacked **several-layer N1** was investigated by a cyclic voltammetry (CV) measurement. In this case the concentration of **L1** was 0.75 mM and it was sprinkled to the air/liquid interface of the subphase (LB trough was compressed to be 73.6 cm², 95% of trough area). The reaction system was left undisturbed for 4 hours. In this condition 10 layers of **single-layer N1** (= **several-layer N1**) covered the surface and the surface pressure became 3.73 mN/m. Then it was transferred to HOPG substrate in LS manner for 7 times at the same surface pressure (ideally 70 layers of **single-layer N1** was modified to the substrate = stacked **several-layer N1**).

  Figure 2-12-3(b) shows a CV result of stacked **several-layer N1** and it represents oxidation potential of 0.60 V (vs Ag⁺/Ag) of stacked **several-layer N1**. Actually this potential is almost the same as another bis(dipyrrinato)zinc(II) complex[18], so that it also supports the formation of bis(dipyrrinato)zinc(II) complex motif in stacked **several-layer N1**. We can observe irreversible peak in this measurement and the peak current decreases in proportion to scan cycles, suggesting the decomposition of Bis(dipyrrinato)zinc(II) complex motif in the nanosheet.
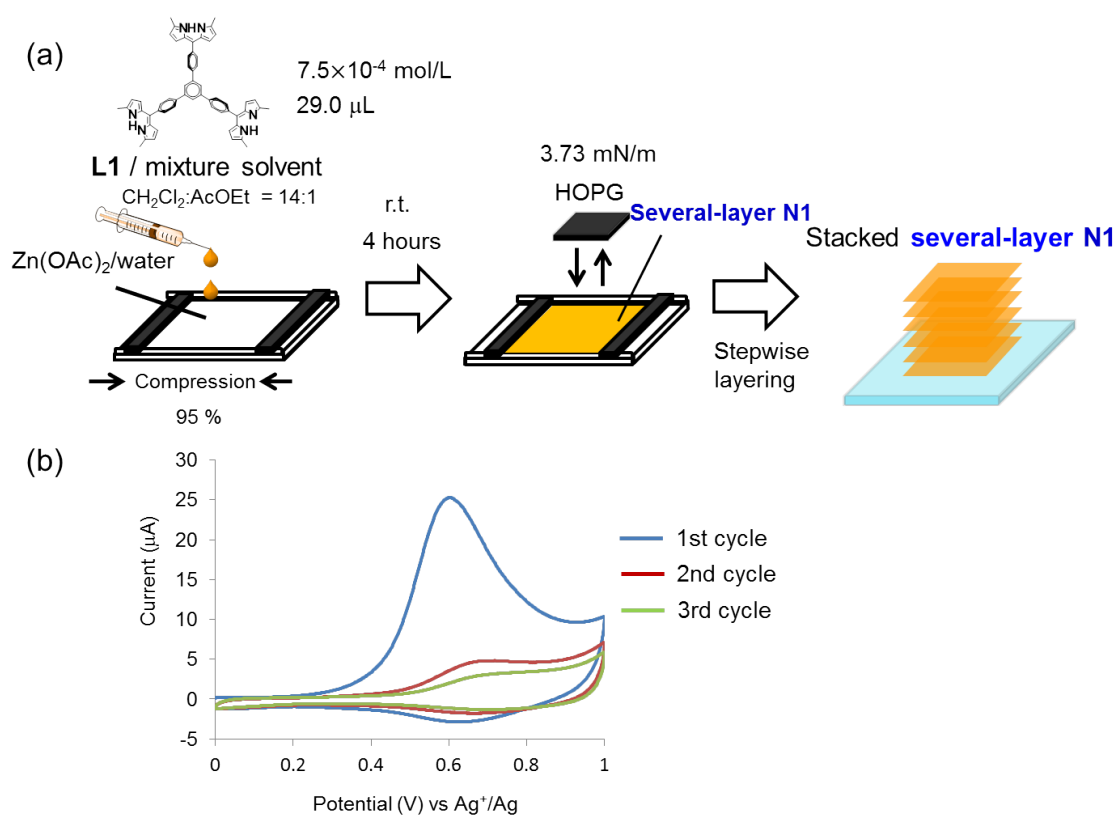
Figure 2-13-3 (a) Schematic illustration of layering **several-layer N1** on a HOPG substrate for electrochemical analysis. (b) Cyclic voltammograms of stacked **several-layer N1**. The peak current decreases with the number of measurements processes.

Then in order to demonstrate the introduction of photofunction to the nanosheets, photoelectric conversion ability of bis(dipyrrinato)zinc(II) nanosheets was investigated. This time **single-layer N1**, **several-layer N1**, stacked **single-layer N1** and stacked **several-layer N1** was employed as the active layer of a photoanode. At first **several-layer N1** was deposited to a gold substrate for photocurrent measurements. 7.4×10^{-5} mol/L **L1** of dichloromethane solution (20 μL) was sprinkled gently to the interface of aqueous solution of zinc acetate in 50-mL glass vial (4.0 cm in diameter). 4 layers of the nanosheets were ideally fabricated at the interface in this case. After 4 hours reaction, **several-layer N1** was transferred to an Au substrate in Langmuir–Schäfer manner.

The photoelectric conversion measurement was performed by three-electrode system as shown in Figure 2-13-4(a). Triethanolamine (TEOA) was added to an electrolyte solution as a sacrificial electron donor and applied potential was set to 0 V for avoiding decomposition of **several-layer N1**. Figure 2-13-4 (b) reveals the anodic photocurrent of **several-layer N1** on irradiation with 500-nm light corresponding to absorption maximum of the nanosheets. Actually, this is the first report of photoelectric conversion using bis(dipyrrinat)zinc(II) complex sensitizer and suggests the possibility of photofunction introduction to the nanosheets. The photocurrent decreased on irradiation with other wavelength light, 450 nm, 550 nm and 600 nm. These results suggest that the observed photocurrent is derived from the photoactive bis(dipyrrinato)zinc(II) complex moiety in **several-layer N1**.

(a)

Counter Electrode (Pt)   Reference Electrode (Ag)

N1 on substrate = Working electrode

Photoirradiation (500nm)

(b)

500-nm light irradiation

On

Off

Photocurrent (nA)

Time (s)

(c)

450-nm light irradiation

On

Off

Photocurrent (nA)

Time (s)

(d) 550-nm light irradiation

(e) 600-nm light irradiation
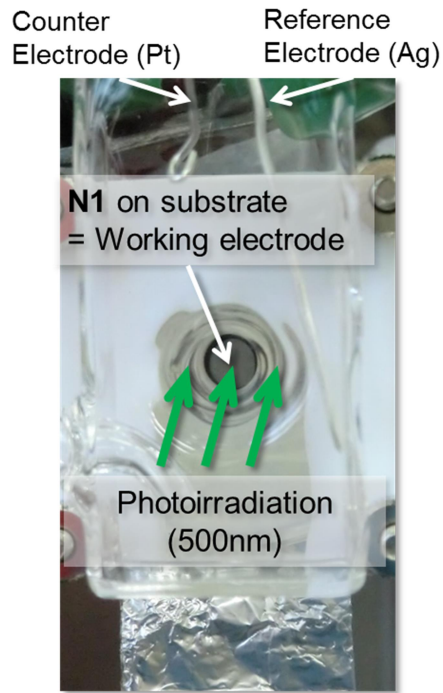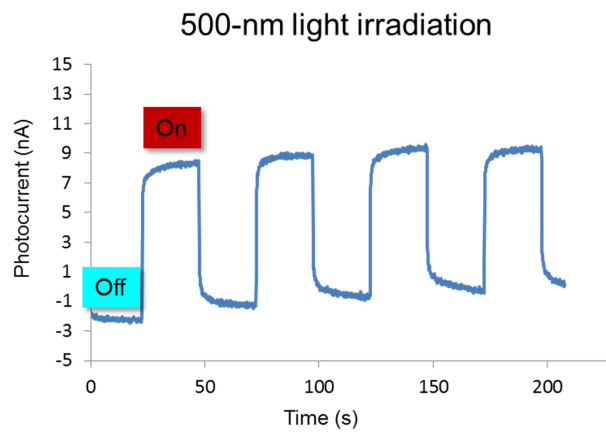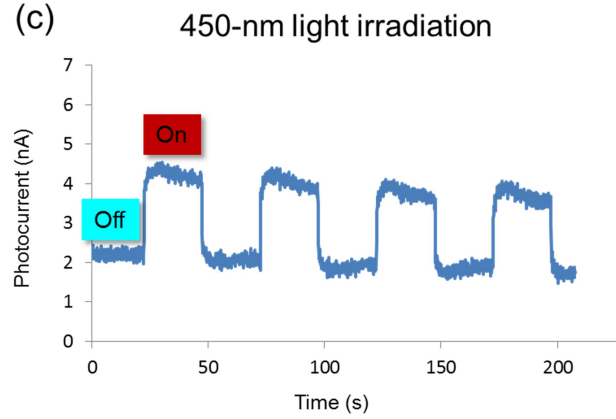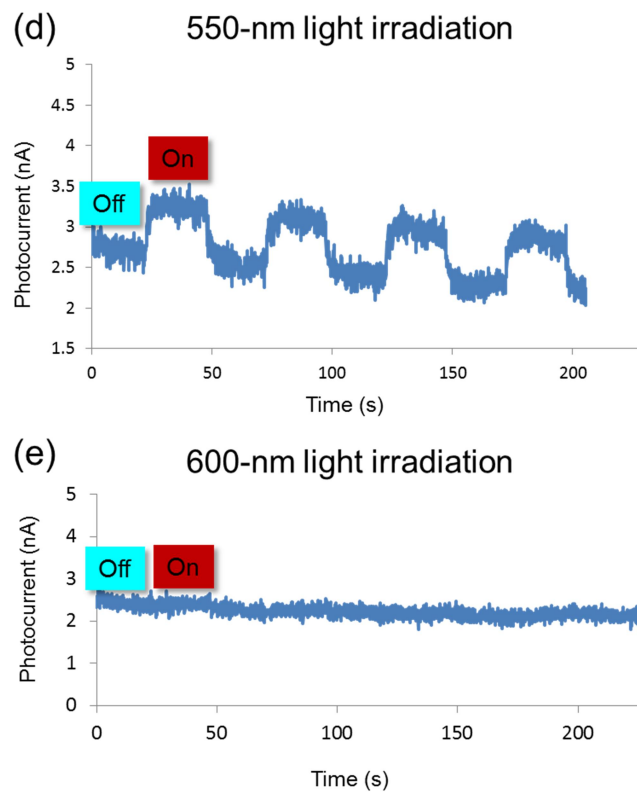
Figure 2-13-4 (a) Photographs of three-electrode photoelectric conversion system. The cell is filled with an electrolyte solution during the measurements. The incident light is illuminated in the direction vertical to the working electrode substrate. (b) Anodic current response of **several-layer N1** on Au substrate with 500-nm light irradiation corresponding to the maximum absorption of **N1**. (c)-(e) Anodic current response on irradiation with 450-nm, 550-nm and 600-nm light.

Then at next, I selected transparent SnO_2 as a deposited substrates and working electrode in consideration of UV/vis absorption measurements. Figure 2-13-5 represents the anodic photocurrent generation ability of **several-layer N1** the same as the nanosheets on Au substrates. This time the nanosheets were transferred to SnO_2 substrates with the same condition as Figure 2-13-4. **Several-layer N1** on SnO_2 produced 36 nA photocurrent whereas on Au produced 10 nA. The superior photocurrent generation of **several-layer N1** on SnO_2 substrate may be derived from the larger amount of deposited **several-layer N1** than that on Au substrate.
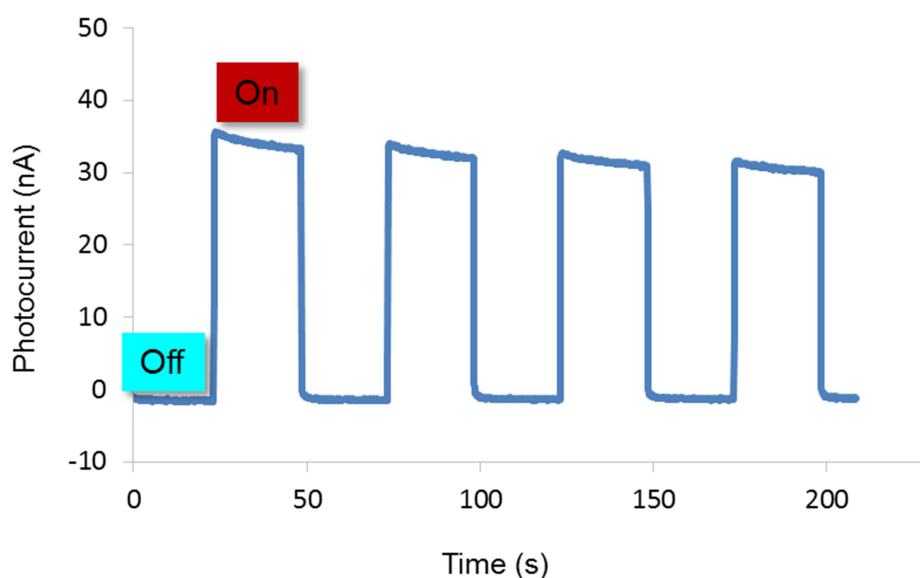
Figure 2-13-5 Anodic current response of **several-layer N1** on a SnO_2 substrate with 500-nm light irradiation corresponding to the maximum absorption of **N1**.

The action spectrum reveals that photocurrent of **several-layer N1** was maximized with 500-nm light irradiation (Figure 2-13-6) corresponding to the maximum absorption of **several-layer N1**. The photocurrent decreased and no response was observed with irradiation of $\lambda < 420$ nm or $\lambda > 560$ nm, where **several-layer N1** negligibly absorbs the light. When the system lacked the nanosheets or TEOA, no photocurrent response was detected. These results ensure the observed photocurrent is just derived from the photoactive moiety of bis(dipyrrinato)zinc(II) CONASHs.
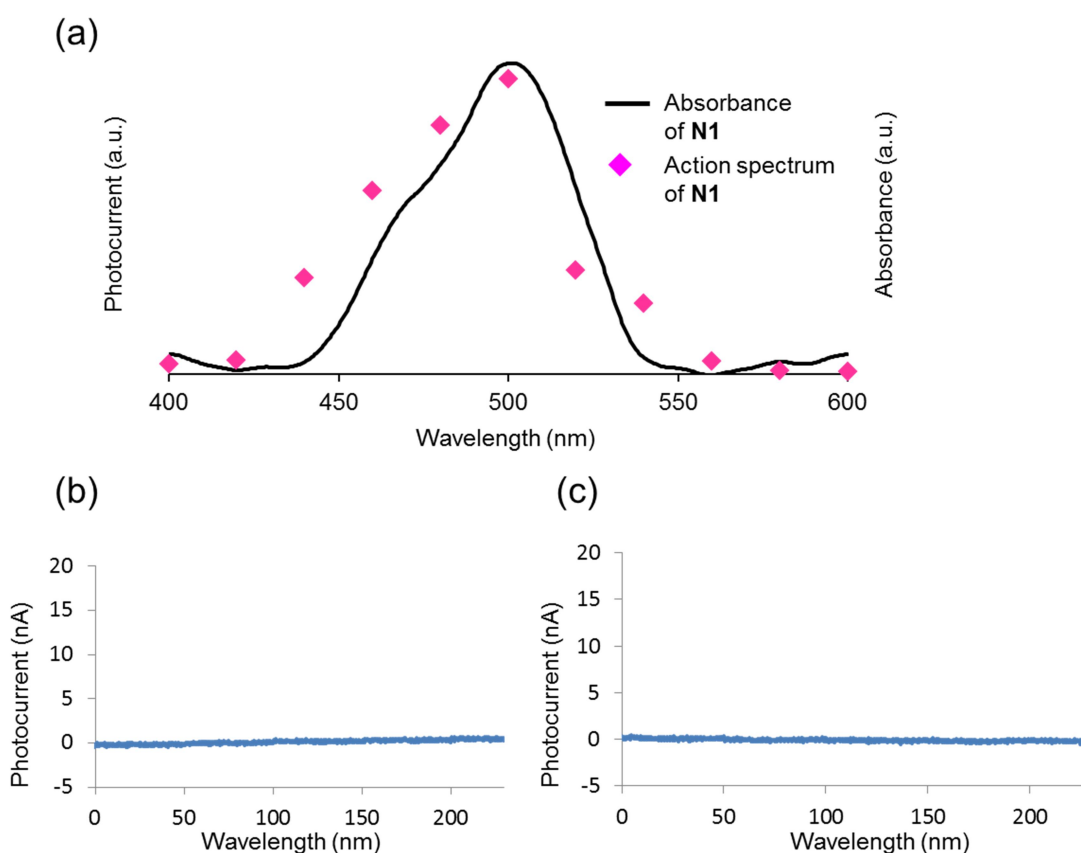
Figure 2-13-6 (a) Action spectrum for the photocurrent generation and absorption spectrum of **N1**. (b) Control experiment without **N1**. (c) Control experiment without TEOA. The irradiation pattern is the same as Figure 2-13-5.

Figure 2-13-7 represents the illustration of photocurrent generation mechanism of **N1**. HOMO level of TEOA is referred from reported paper[19] and both the HOMO and LUMO levels of the nanosheets are estimated from previous electrochemical reports of bis(dipyrrinato)zinc(II) complex[18] (0.39 V vs Fc$^+$/Fc for oxidation potential and -2.09 V vs Fc$^+$/Fc for reduction potential). The estimated energy gap between the HOMO and the LUMO of **N1** matches well to the UV/vis light absorption result. 500-nm light irradiation encourages electrons excitation in **N1** and the excited electrons move to working electrode (Au or SnO$_2$. **N1** is deposited onto the working electrode substrate and its potential is set to 0 V vs Ag$^+$/Ag). Lacking electrons in **N1** are supplied from TEOA which acts as a sacrificial electron donor, and at the same time it receives an electron from counter electrode. The following electron flow generates the anodic photocurrent on photoirradiation with **N1**'s absorption maximum wavelength.
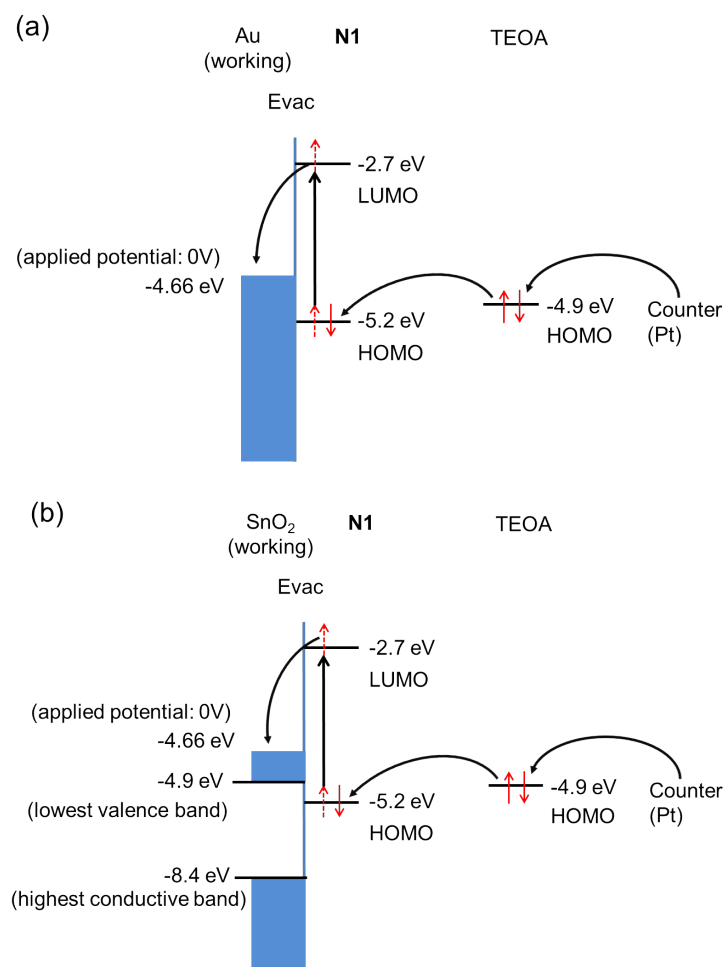
Figure 2-13-7 Illustration of photocurrent generation scheme. (a) **Several-layer N1** transferred to Au substrate. (b) **Several-layer N1** transferred to SnO$_2$ substrate.

2-13-4 Conversion efficiency

  I then studied the photoelectric conversion efficiency of **N1**. Figure 2-13-8(a) shows relationship between the quantum yield of the photoelectric conversion and thickness of **N1**. **Single-layer N1** exhibits the highest value (0.86%), which decreases gradually with increasing thickness of **N1**, leading to negligible photoresponses at thicknesses of over ~300 layers. Figure 2-13-8(b) also reveals the maximum photocurrent is located at ~100-150 layers. In order to demonstrate the superiority of **N1**, two types of mononuclear bis(dipyrrinato)zinc(II) complex sensitizers were prepared: a plain zinc(II) complex **M2**, which was dropcasted onto a SnO_2 electrode to form a physisorbed film (Figure 2-13-8(c)) and **M3** with carboxy groups, which underwent chemisorption onto a SnO_2 surface to form a self-assembled monolayer (Figure 2-13-8(d)). These two photoanodes resulted in much lower conversion efficiencies (0.030 and 0.069%), thereby justifying the superiority of a bottom-up CONASH **N1** over conventional molecular films. The nanosheet structure of **N1** affords appropriate porosity and suppresses molecular aggregation; these features presumably make N1 a better sensitizer. In addition, the coexistence of insolubility (to avoid redissolution into media) and manipulability (to facilitate deposition and layering) of **N1** is also advantageous for potential applications.
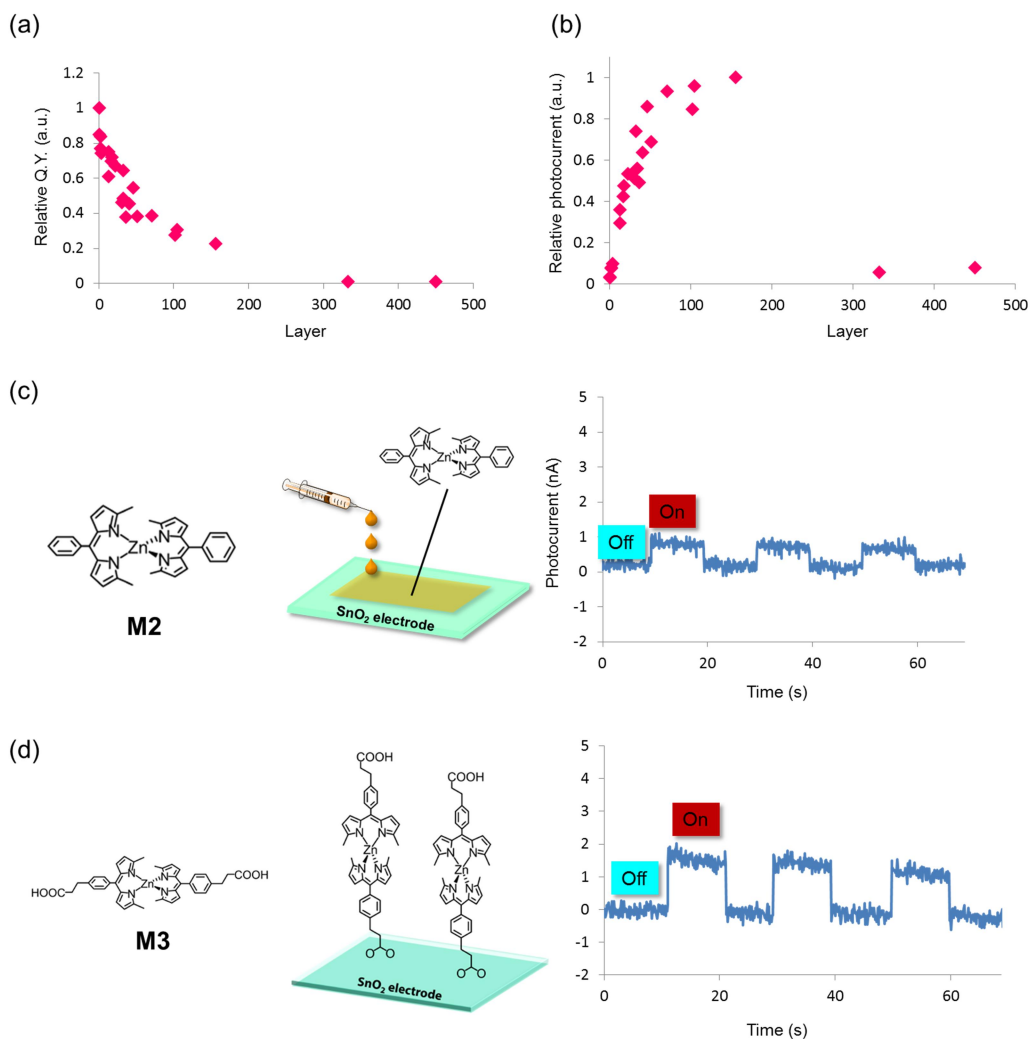
Figure 2-13-8 (a) Relationship between relative quantum yield (Q.Y.) and the thickness of **N1** on irradiation with 500-nm light. The highest Q.Y. (0.86% by **single-layer N1**) is taken as the standard. Layer numbers were estimated from absorbance of each **N1** and single-layer nanosheet (Figure 2-13-2). (b) Relationship between relative photocurrent and thickness of **N1** on irradiation with 500-nm light. The photocurrent was corrected by the intensity of incident light. The highest photocurrent (39 nA with an incident light intensity of 0.16 mW by 154-layer **N1**) is taken as the standard. (c) Chemical structure of mononuclear complex **M2** and its anodic current response on irradiation of the **M2**-physisorbed SnO_2 electrode with intermittent 500-nm light. Light intensity, 0.19 mW. This measurement produced a quantum efficiency of 0.030%. (d) Chemical structure of mononuclear complex **M3** and its anodic current response on irradiation of the **M3**-chemisorbed SnO_2 electrode with intermittent 500-nm light. Light intensity, 1.8 mW. This measurement produced a quantum efficiency of 0.069%.

For investigating the durability of the system, the photocurrent responsibility was measured for 136 cycles of on-off switching. Figures 2-13-9(a)-(c) reveal the photocurrent decreasing for the first 60 cycles and then showing stable anodic current (5.4 nA). The stable photocurrent suggests that decomposition of photoactive bis(dipyrrinato)zinc(II) unit is not a reason of the photocurrent decrease. Then in order to investigate whether TEOA diffusion contributes to the photocurrent decrease, after 136 cycles test I shook the reaction system and observed the photocurrent generation (Figure 2-13-9(d)). This time **several-layer N1** produced slightly fewer photocurrent than that before shaking the system, so it ensured the TEOA diffusion did not cause the photocurrent decrease. The main reason of the decrease is considered to be derived from the removal of **several-layer N1** from SnO_2 substrate. 4 layers of stacked nanosheets were transferred to the substrate in this case so that some part of the nanosheets is deposited weekly and it can be peeled off easily from the substrate. These experimental results indicate that at first 60 cycles weakly deposited nanosheets were removed to show photocurrent decrease, then the stable photocurrent was achieved after the detachment of the nanosheets stopped.
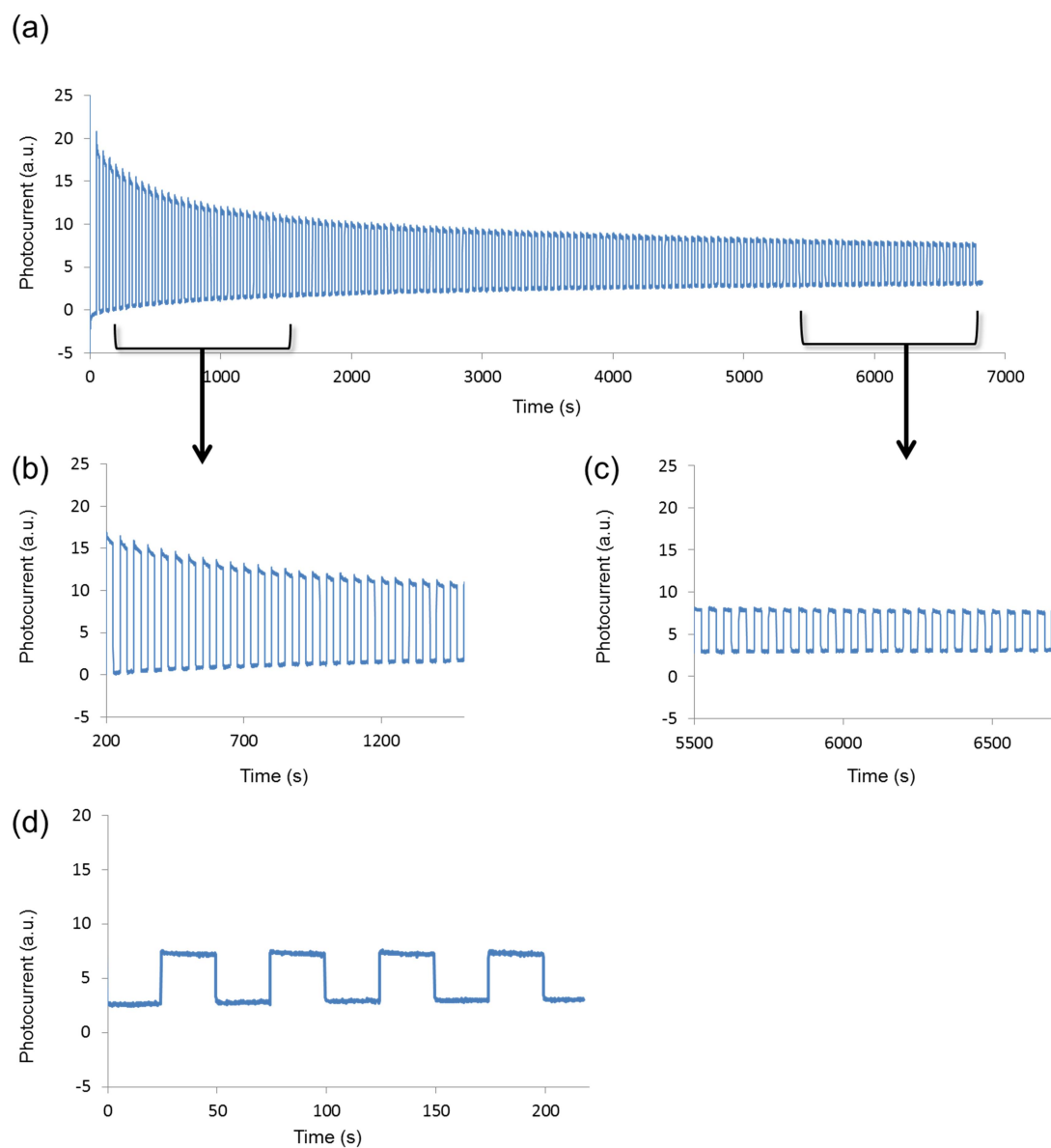
Figure 2-13-9 (a) Anodic current response of **several-layer N1** on a SnO_2 substrate with 500-nm light irradiation with 136 on-off cycles. (b) Close-up from 200 sec to 1500 sec. (c) Close-up from 5500 sec to 6700 sec. (d) Photocurrent of **several-layer N1** after shacking the system. The measurement was followed by (a). It produced ca. 4.6 nA of anodic current.

2-14 Summary

  This chapter describes the fabrication of bis(dipyrrinato)zinc(II) nanosheets and its photofunctiolnality. The interfacial synthesis between dipyrrin ligand and zinc ions produces multi-layer, several-layer and single-layer coordination nanosheets (**multi-layer N1**, **several-layer N1** and **single-layer N1**). Their morphology was observed by optical microscopy, SEM, TEM and AFM to show flat two-dimensional sheet-like texture. **Single-layer N1** possesses 1.2 nm thickness and its size reaches more than 10 μm which is larger than other CONASHs. The constituent elements of bis(dipyrrinato)zinc complex in the nanosheets are revealed by UV/vis spectroscopy and XPS. SAED measurements identify their hexagonal in-plane periodicity to be 3.6 nm which is consistent with optimized structure. The nanosheets photofunction was demonstrated by photocurrent generation. They collect visible light at around 500 nm, and the nanosheets deposited onto SnO_2 substrates show photoelectric conversion ability. The conversion efficiency is studied to represent highest value at single-layer thickness. **Single-layer N1** exhibits much larger photoelectric conversion efficiency than other conventional films to justify the superiority of a bottom-up CONASH.

2-15 References

1) (a) Loudet, A.; Burgess, K. *Chem. Rev.* **2007**, *107*, 4891-4932.

(b) Ulrich, G.; Ziessel, R.; Harriman, A. *Angew. Chem., Int. Ed.* **2008**, *47*, 1184-1202.

2) Sakamoto, R.; Iwashima, T.; Tsuchiya, M.; Toyoda, R.; Matsuoka, R.; Kögel, J. F.; Kusaka, S.; Hoshiko, K.; Yagi, T.; Nagayama, T.; Nishihara, H. *J. Mater. Chem. A* **2015**, *3*, 15357-15371.

3) Matsuoka, R.; Toyoda, R.; Sakamoto,R.; Tsuchiya, M.; Hoshiko, K.; Nonoguchi, Y.; Nishibori, E.; Kawai, T.; Nishihara, H. *Chem. Sci.* **2015**, *6*, 2853-2858.

4) Béziau, A.; Baudron, S. A.; Rogez, G.; Hosseini, M. W. *Inorg. Chem.* **2015**, *54*, 2032-2039.

5) (a) Kusaka, S.; Sakamoto, R.; Kitagawa, Y.; Okumura, M.; Nishihara, H. *Chem. Asian J.* **2012**, *7*, 907-910.

(b) Kusaka, S.; Sakamoto, R.; Nishihara, H. *Inorg. Chem.* **2014**, *53*, 3275-3277.

6) Sakamoto, R.; Hoshiko K.; Liu Q.; Yagi T.; Nagayama T.; Kusaka S.; Tsuchiya M.; Kitagawa Y.; Wong W.-Y.; Nishihara H. *Nature Commun.* **2015**, *6*, 6713-6721.

7) Wang Z.; Lu P.; Chen S.; Gao Z.; Shen F.; Shang W.; Xu Y.; Kwok H. S.; Ma Y. *J. Mater. Chem.* **2011**, *21*, 5451-5456.

8) Micheal, M.-C. L.; Gregory, C. F. J. *Am. Chem. Soc.* **2002**, *124*, 4572-4573.

9) Tsuchiya, M.; Sakamoto, R.; Kusaka, S.; Kitagawa Y.; Okumura, M.; Nishihara, H. *Chem.Commun.* **2014**, *50*, 5881-5883.

10) Qin, W.; Baruah, M.; Van der Auweraer, M.; De Schryver, F. C.; Boens, N.; *J. Phys. Chem. A* **2005**, *109*, 7371-7384.

11) Nagaoka, S.; Horiuchi, K.; Shikishima, M.; Nakajima, A. *J. Phys. Chem. C* **2011**, *115*, 24215-24220.

12) Karweik, D. H.; Winograd, N. *Inorg. Chem.* **1976**, *15*, 2336-2342.

13) Bureekaew, S.; Shimomura, S.; Kitagawa, S. *Sci. Technol. Adv. Mater.* **2008**, *9*, 1-12.

14) Tsunomori, F.; Ushiki, H. *Phys. Let. A* **1999**, *258*, 171-176.

15) Kubin, R. F.; Fletcher, A. N. *J. Luminescence.* **1982**, *27*, 455-462.

16) Kambe, T.; Sakamoto R.; Hoshiko, K.; Takada, K.; Ryu, J.-H.; Sasaki, S.; Kim, J.; Nakazato, K.; Takata, M.; Nishihara, H.; *J. Am. Chem. Soc.* **2013**, *135*, 2462-2465.

17) Takada, K.; Sakamoto, R.; Yi, S.-T.; Katagiri, S.; Kambe, T.; Nishihara, H. *J. Am. Chem. Soc.* **2015**, *137*, 4681-4689.

18) Kusaka, S. Ph. D. thesis, The University of Tokyo, Tokyo, Japan, **2013**.

19) Driscoll, P. F.; Douglass, E. F.; Phewluangdee , M. J.; Soto, E. R.; Christopher, G. F. C.; MacDonald, J. C.; Lambert, C. R.; McGimpsey. W. G. *Langmuir*, **2008**, *24*, 5140-5145.

Chapter 3

Bis(acetylacetonato)copper(II) nanosheet

本章については、5 年以内に雑誌等で刊行予定のため、非公開。

本章については、5 年以内に雑誌等で刊行予定のため、非公開。

Chapter 4

Concluding remarks

The present thesis mentions the studies on designing and demonstration of bottom-up coordination nanosheets' function. I selected two kinds of metal complexes as components of nanosheets to achieve this aim: bis(dipyrrinato)zinc(II) and bis(acetylacetonato)copper(II). Their functions are successfully introduced to the nanosheets to fabricate various functional coordination nanosheets.

In the research in Chapter 2, photofunctional bottom-up coordination nanosheets containing the photoactive bis(dipyrrinato)zinc complex motif are fabricated. Multi-layer and single-layer nanosheets are prepared via interfacial synthesis. Spontaneous complexation reaction proceeds between a three-way dipyrrin ligand (1,3,5-tris-[4'-(5-mehyl-1H-pyrrole-2-yl -(5-methyl-2H-pyrrole-2-ylidene)methyl)phenyl]benzene, **L1**) and zinc ions at the interface. The nanosheet is identified using UV/vis spectroscopy and XPS, which reveal the complete formation of the bis(dipyrrinato)zinc complex motif. The single-layer nanosheet is confirmed by AFM via a scratch experiment. The homogenous area of the single-layer nanosheet reaches more than 10 μm on one side, which is significantly large for bottom-up nanosheet materials. Repeated deposition of the single-layer nanosheet on a flat substrate results in its quantitative layering. The nanosheet efficiently collects visible light at around 500 nm, and it can be physisorbed on a transparent SnO_2 to function as an active layer in a photoelectric conversion system. The photofunctionality in the molecule-based bottom-up nanosheet demonstrated herein leads to a significant expansion of the applicability of coordination two-dimensional matters as useful and promising nanomaterials.

In the research in Chapter 3, the coordinatevely unsaturated bis(acetylacetonato)copper(II) complex motif produces bottom-up coordination nanosheet with molecular recognition. Multi-layer and single-layer nanosheets are prepared via interfacial synthesis. Spontaneous complexation reaction proceeds between a three-way acetylacetone ligand (1,3,5-tris-[4'-(3"-acetylacetonato)phenyl]benzene, **L2**) and copper(II) ions at the interface. The IR spectroscopy, SEM/EDS and XPS confirm that the nanosheet is constructed from bis(acetylacetonato)copper(II) complex unit. The single-layer nanosheet is identified by AFM via a scratch experiment.

The size of the single-layer nanosheet is also more than 10 μm, the same as bis(dipyrrinato)zinc(II) nansoheet, suggesting the same coordination characters contribute the large size of the nanosheet. The multi-layer nanosheet exhibits its optical property modulation by modification of coordinating molecules. The nanosheet can recognize the coordinating and non-coordinating molecules to show UV/vis change by immersing in [Fe(tpypy)$_2$]$^{2+}$. This simple modulation of nanosheet property can open up the utility of bottom-up coordination nanosheets.

  In this thesis I describe the successful fabrication of two series of bottom-up coordination nanosheets by using different metal complex components, and it reveals varieties of bottom-up coordination nanosheets. The constructed nanosheets reveal their huge area which is necessary in application. Furthermore, both of them demonstrate various functions different from past bottom-up nanosheets such as photofunction and molecular recognition. These findings will contribute to develop the value of bottom-up coordination nanosheets toward application.

Acknowledgment

Publication List

[Publications related to the thesis]

1. "A photofunctional bottom-up bis(dipyrrinato)zinc(II) complex nanosheet" Ryota Sakamoto, <u>Ken Hoshiko</u>, Qian Liu, Toshiki Yagi, Tatsuhiro Nagayama, Shinpei Kusaka, Mizuho Tsuchiya, Yasutaka Kitagawa, Wai-Yeung Wong, Hiroshi Nishihara, *Nature Commun.* **2015**, *6*, 6713-6721.

R.S. conceived and directed the project. R.S., H.N., K.H. and W.-Y.W. initiated the project. S.K., Q.L. and W.-Y.W. synthesized ligand **L1**. K.H., Q.L. and T.N. performed the fabrication of **N1** and **M1**. T.N. and M.T. synthesized **M2** and **M3**, respectively. Y.K. optimized the three-dimensional lattice of multi-layer **N1** at the molecular mechanics level of theory. K.H. conducted the characterization of **N1**. T.Y. and K.H. investigated the photoelectric conversion of **N1**, **M2** and **M3**. R.S. and K.H. co-wrote the manuscript.

[Publications not related to the thesis]

1. "The coordination nanosheet (CONASH)" Ryota Sakamoto, Kenji Takada, Xinsen Sun, Tigmansu Pal, Takamasa Tsukamoto, Eunice Jia Han Phua, Amalia Rapakousiou, <u>Ken Hoshiko</u>, Hiroshi Nishihara, *Coord. Chem. Rev.* **2016**, *320-321*, 118-128.

2. "Redox Control and High Conductivity of Nickel Bis(dithiolene) Complex π-Nanosheet: A Potential Organic Two-Dimensional Topological Insulator" Tetsuya Kambe, Ryota Sakamoto, Tetsuro Kusamoto, Tigumasu Pal. Naoya Fukui, Ken Hoshiko, Takahiro Shimojima, Zhengfei Wang, Toru Hirahara, Kyoko Ishizaka, Shuji Hasegawa, Feng Liu, Hiroshi Nishihara, *J. Am. Chem. Soc.* **2014**, *136*, 14357-14360.

3. "New aspects in bis and tris(dipyrrinato)metal complexes: bright luminescence, self-assembled nanoarchitectures, and materials applications" Ryota Sakamoto, Toshiki Iwashima, Tsuchiya Mizuho, Ryojun Toyoda, Ryota Matsuoka, Julius F. Koegel, Shinpei Kusaka, <u>Ken Hoshiko</u>, Toshiki Yagi, Tatsuhiro Nagayama, Hiroshi Nishihara, *J. Mater. Chem. A* **2015**, *3*, 15357-15371

4. "Bis(dipyrrinato)metal(II) coordination polymers: Crystallization, exfoliation into single wires, and electric conversion ability" Ryota Matsuoka, Ryojun Toyoda, Ryota Sakamoto, Mizuho Tsuchiya, <u>Ken Hoshiko</u>, Tatsuhiro

Nagayama, Yoshiyuki Nonoguchi, Kunihisa Sugimoto, Eiji Nishibori, Tsuyoshi Kawai, Hiroshi Nishihara, *Chem. Sci.* **2015**, *6*, 2853-2858.

5. "Geometric and Electrochemical Properties of Complexes Consisting of Two Aminonaphthoquinone-bound Schiff-base Ligands and Mn^{II}, Fe^{II}, Ni^{II}, Cu^{II}, or Zn^{II}" Yuta Hasegawa, Haruki Nakamura, Yohei Hattori, <u>Ken Hoshiko</u>, Tetsuro Kusamoto, Masaki Murata, Shoko Kume, and Hiroshi Nishihara, *Polyhedron* **2015**, 86, 111-119.